On the laminar–turbulent transition of the rotating-disk flow: the role of absolute instability

Shintaro Imayama[1], **P. Henrik Alfredsson**[1] **and R. J. Lingwood**[1,2],†

[1]Linné Flow Centre, KTH Mechanics, SE-100 44 Stockholm, Sweden

[2]Institute of Continuing Education, University of Cambridge, Madingley Hall, Madingley, Cambridge CB23 8AQ, UK

This paper describes a detailed experimental study using hot-wire anemometry of the laminar–turbulent transition region of a rotating-disk boundary-layer flow without any imposed excitation of the boundary layer. The measured data are separated into stationary and unsteady disturbance fields in order to elaborate on the roles that the stationary and the travelling modes have in the transition process. We show the onset of nonlinearity consistently at Reynolds numbers, R, of $\sim$510, i.e. at the onset of Lingwood's (*J. Fluid Mech.*, vol. 299, 1995, pp. 17–33) local absolute instability, and the growth of stationary vortices saturates at a Reynolds number of $\sim$550. The nonlinear saturation and subsequent turbulent breakdown of individual stationary vortices independently of their amplitudes, which vary azimuthally, seem to be determined by well-defined Reynolds numbers. We identify unstable travelling disturbances in our power spectra, which continue to grow, saturating at around $R = 585$, whereupon turbulent breakdown of the boundary layer ensues. The nonlinear saturation amplitude of the total disturbance field is approximately constant for all considered cases, i.e. different rotation rates and edge Reynolds numbers. We also identify a travelling secondary instability. Our results suggest that it is the travelling disturbances that are fundamentally important to the transition to turbulence for a clean disk, rather than the stationary vortices. Here, the results appear to show a primary nonlinear steep-fronted (travelling) global mode at the boundary between the local convectively and absolutely unstable regions, which develops nonlinearly interacting with the stationary vortices and which saturates and is unstable to a secondary instability. This leads to a rapid transition to turbulence outward of the primary front from approximately $R = 565$ to 590 and to a fully turbulent boundary layer above 650.

Key words: absolute/convective instability, boundary layer stability, transition to turbulence

1. Introduction

The laminar–turbulent transition of the incompressible rotating-disk flow without any imposed flow is discussed. For an infinite rotating disk in otherwise quiescent fluid, von Kármán (1921) derived an exact similarity solution of the governing equations for the laminar boundary layer. The Rossby number for the von Kármán flow is $Ro =$

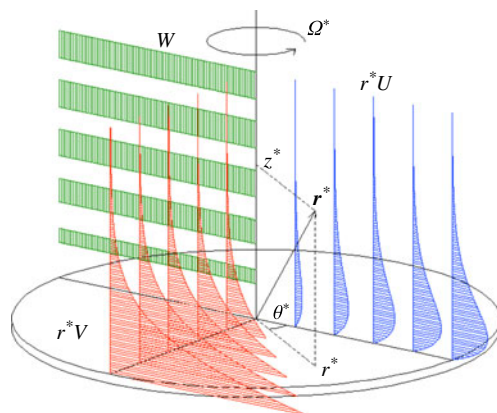† Email address for correspondence: lingwood@mech.kth.se

FIGURE 1. A sketch of the von Kármán boundary layer on a rotating disk showing the mean velocity profiles (in a laboratory frame).

-1, as defined, for example, by Lingwood & Garrett (2011). The velocity distribution in the boundary layer is three-dimensional and has an inflection point in the radial direction. Figure 1 shows the laminar velocity profiles where $U = U^*/(r^*\Omega^*)$, $V = V^*/(r^*\Omega^*)$, $W = W^*/(\nu^*\Omega^*)^{1/2}$ are non-dimensional radial, azimuthal and axial mean velocities, respectively. U^*, V^*, W^* are the mean radial, azimuthal and axial velocities, r^* is radius of the disk at the measurement position, z^* is the wall-normal height from the disk surface, Ω^* is the rotational speed of the disk, ν^* is the kinematic viscosity of the fluid, θ^* is the angular position, and $*$ denotes a dimensional quantity.

The inflectional nature of the mean velocity leads to inviscid instability, usually called 'cross-flow instability'. Local stability analysis (e.g. Malik, Wilkinson & Orszag 1981) shows that the critical Reynolds number for convective instability of the stationary mode (i.e. fixed with respect to the rotating disk) within this so-called Type-I cross-flow instability is about $R = 287$, where the Reynolds number is $R = r^*(\Omega^*/\nu^*)^{1/2}$. The flow on the rotating disk is also unstable to a so-called Type-II viscous instability. Type-II *stationary* disturbances have higher critical Reynolds number and smaller spatial growth rates than Type-I stationary disturbances. However, the Type-II *travelling* modes can have significantly lower critical Reynolds numbers than both stationary and travelling Type-I modes. Faller (1991) shows that the critical Reynolds number of Type-II travelling modes is $R = 69.4$ where the wave angle is $-19.0°$. The mode with maximum spatial growth rate is a Type-I mode that has large negative frequency in the rotating frame (Hussain, Garrett & Stephen 2011), i.e. a disturbance that is travelling significantly slower than the rotating disk. However, as shown in many studies (e.g. in the flow visualization of Kohama 1984), the dominant observed structures in the convectively unstable region of the boundary layer are stationary (cross-flow Type-I) spiral vortices; typically 28–32 are observed. These vortices are triggered by small, but unavoidable roughnesses on the disk surface, which continuously excite the stationary mode. Travelling modes are not naturally excited repeatably and continuously reinforced in the same way, and so (despite some such modes having lower critical Reynolds numbers and higher growth rates) their contribution to the disturbance field and their role in the transition process are often overlooked.

The rotating-disk flow is considered to be a good model for comparison with swept-wing boundary-layer flows (e.g. Gregory, Stuart & Walker 1955) due to their

similar velocity profiles and cross-flow instability. However, the rotating-disk flow has azimuthal periodicity that is not reflected as spanwise periodicity in the swept-wing flow, and observations of the rotating-disk flow differ from swept-wing flows in at least one important way, namely the relatively small variation in Reynolds number observed for laminar–turbulent transition across different facilities. This difference is clearly shown in flow visualizations for which the rotating-disk flow exhibits a sharp circular demarcation of turbulent breakdown in the transitional region (e.g. Kohama 1984) whereas for swept-wing boundary-layer flows (e.g. Dagenhart & Saric 1999) the transition zone zigzags in the spanwise direction.

A recent experimental study of the rotating-disk flow (Imayama, Alfredsson & Lingwood 2013) suggested that the transition Reynolds number, R_t, defined as the onset of the nonlinearity is $515 \pm 1\%$, independent (within the ranges spanned by available data) of background noise level, edge condition, and edge Reynolds number R_{edge}, where $R_{edge} = r_d^*(\Omega^*/\nu^*)^{1/2}$, r_d^* being the finite radius of the disk.

Lingwood (1995) found that the convectively unstable rotating-disk boundary layer becomes locally absolutely unstable in the radial direction for certain travelling disturbances (i.e. with negative frequency in the rotating frame) above $R_{CA} = 507$, where R_{CA} denotes the critical Reynolds number for the absolute instability. She suggested that the absolute instability at a fixed radial position is the trigger for the onset of nonlinearity at that location, the first step of the transition process. She also confirmed experimentally (Lingwood 1996) the absolute instability above ∼507 by introducing a travelling wavepacket into the boundary layer and observing that the trailing edge becomes fixed (radially) in space as it approaches R_{CA}. Lingwood (1997*b*) showed that a model swept-wing boundary-layer flow exhibits local chordwise absolute instability for certain sets of parameters. However, unlike the absolute instability of the rotating-disk flow, she suggested for swept-wing flows that, due to the lack of periodicity in the spanwise direction (analogous to the azimuthal periodicity present for the rotating-disk configuration, which creates a semi-closed flow), unidirectional absolute instability of swept-wing flows may be less physically significant and that 'laminar–turbulent transition may still be a convective process'.

Davies & Carpenter (2003) conducted direct numerical simulations (DNS) of the linearized Navier–Stokes equations, which unlike local stability analysis account for spatial variation of the flow, and found that the rotating-disk boundary-layer flow is linearly globally stable, in contrast to Lingwood's (1996) observations. Davies & Carpenter (2003) instead suggested that the convective behaviour eventually prevails even for strongly locally absolutely unstable regions. To explain this contradiction, Pier (2003) showed that a nonlinear approach provides, via a subcritical mechanism, a nonlinear global instability (provided that background disturbances are sufficient) at the location for the onset of local absolute instability, resulting in a self-sustained finite-amplitude disturbance that is subject to secondary instability.

Another approach was taken by Healey (2010) who, using the linearized complex Ginzburg–Landau equation, proposed that if a finite-disk configuration is considered (as applies to all physical experiments) then the local absolute instability gives rise (via a supercritical mechanism) to linear global instability leading directly to a nonlinear global mode regardless of the background disturbance level. Healey pointed out that Davies & Carpenter (2003) disregarded upstream propagation of waves from the edge boundary as a spurious numerical artifact and stopped the calculations before such waves reached the domain of interest. Adding a nonlinear term into the model, Healey (2010) also argued that as the transition Reynolds number approaches the Reynolds number at the edge, the flow is stabilized and he suggested that this

effect explains the scatter, albeit small, observed in the earlier experimental transition Reynolds numbers. However, from the experiments of Imayama *et al.* (2013), with various edge conditions and edge Reynolds numbers, it was concluded that these different conditions did not affect the transition Reynolds number significantly. Instead, Imayama *et al.* (2013) showed that the scatter in the reported transition Reynolds numbers could be explained by the different definitions of transition used by various researchers, rather than a nonlinear stabilizing effect brought about by the proximity of the edge of the disk. Nevertheless, application of a consistent definition for transition to previous experimental results, as attempted by Imayama *et al.* (2013), showed that the transition Reynolds number is highly reproducible across different facilities, which may lend support to Healey's (2010) primary suggestion that the finite radius of the disk creates a (supercritical) linear global instability leading directly to a nonlinear global mode irrespective of differences in background noise levels.

The late stage of laminar–turbulent transition has also been investigated in previous studies. Kobayashi, Kohama & Takamadate (1980) and Wilkinson & Malik (1985) observed secondary instability of the primary stationary vortices characterized as a 'kink' in single-realization time series of the azimuthal velocity component just before the turbulent breakdown region. Kohama, Suda & Watanabe (1994) fixed a hot-wire probe on the disk surface and investigated disturbances travelling with respect to the disk in the transition region. They found two different travelling frequency components, one at 150 Hz and the other at 3.5 kHz, and concluded that the higher frequency component was due to the secondary instability captured as ring-like structures by the visualization technique just before the turbulent breakdown. Using a theoretical approach, Balachandar, Streett & Malik (1992) suggested that the root-mean-square amplitude of the primary stationary disturbances must be $\sim 9\%$ of the local disk velocity to trigger the secondary instability at $R = 500$ and that the travelling secondary instability appears as a pair of counter-rotating vortices. However, recent studies suggest (e.g. Lingwood 1996; Healey 2010; Garrett, Harris & Thomas 2012; Harris, Garrett & Thomas 2012; Imayama *et al.* 2013) that there may be an alternative (lower Reynolds number) transition mechanism for sufficiently rough disks. Such rough-disk flows may show early nonlinearity and secondary instability, and turbulent breakdown (i.e. for $R < 507$ below the onset of the absolute instability); Imayama *et al.* (2013) distinguished past experimental studies using hot-wire anemometry as either clean-disk or rough-disk experiments, see their table 3.

The exact nature of the laminar–turbulent transition of the rotating-disk flow is, however, still not fully understood, in particular, to what extent the absolute instability, travelling disturbances and secondary instabilities are involved in the transition process. An important factor in the present study is to try to distinguish a primary *travelling* global mode and its secondary instability, or otherwise, from the more easily observed *stationary* vortices; as the local absolute instability occurs for travelling modes, consideration only of the latter is likely to obscure the global instability behaviour. In this way, it is possible to draw some comparisons with the subcritical and supercritical travelling global-instability mechanisms described by Pier (2003) and Healey (2010), respectively, where the location of the steep-fronted global mode is controlled by the onset of absolute instability and the turbulent breakdown is triggered by secondary instability of the primary global mode; see also Viaud, Serre & Chomaz (2011).

The aim of this study is to add to current understanding via careful experimental investigation, using hot-wire anemometry, of the laminar–turbulent transition process for a 'clean' disk, and to compare with theoretical, numerical and other experimental

studies. The experimental setup is described in § 2. The experiments have been performed without deliberate forcing of the boundary layer, i.e. without any artificial excitation (e.g. roughness or impulsive jet). The results are presented in § 3. In particular, the disturbances are decomposed into stationary and unsteady components and the behaviour of each is investigated. Finally, the conclusions are given in § 4.

2. Experimental setup

The experimental setup is identical to the one in Imayama, Alfredsson & Lingwood (2012) and Imayama *et al.* (2013), see Imayama *et al.*'s (2012) figure 1, and is a modified version of the setup used by Lingwood (1996). The glass disk with a thickness of 24 mm and a diameter of 474 mm is mounted on an aluminium-alloy disk fixed by eight aluminum clamps. The edge of the glass disk is ground down approximately 1.5 mm with a 45° angle giving a working radius of the glass disk of $r_d^* = 235.5$ mm, see the sketch of Imayama *et al.*'s (2013) figure 1(*c*). Around the disk a wooden stationary board with outside diameter of 900 mm is mounted to minimize noise contamination. The horizontal gap between the wooden plate and the disk is less than 1 mm and vertically the disk surface and the plate are approximately flush.

Measurements of the azimuthal velocity are performed by hot-wire anemometry using the same setup and techniques as Imayama *et al.* (2012, 2013). Table 1 shows the experimental conditions in the present work and PP02, PP04–12 and IP02 are identical to the data used in Imayama *et al.* (2012). The data PP02, PP04, PP06, PP08, PP10, PP12, IP01 and IP02 in the present study are also used in Imayama *et al.* (2013). Note, however, that the case labels used in table 1 are different from those used in the other two papers. Two methods were used for varying the Reynolds number: (*a*) varying the rotational disk speed and keeping the probe at a fixed radial position (PP01–12); and (*b*) varying the radial position of the probe at a fixed rotational disk speed (IP01–02). For cases PP01–12 measurements of the azimuthal velocity profile were made at each Reynolds number, whereas for IP01 and IP02 measurements were only taken at a non-dimensional height $z = 1.3$, where $z = z^*(\Omega^*/\nu^*)^{1/2}$.

The non-dimensional boundary-layer thickness is given as $\delta_{95} = \delta_{95}^*(\Omega^*/\nu^*)^{1/2}$, where δ_{95}^* is defined as the wall-normal position where the azimuthal velocity is 5 % of the local disk velocity, V_w^*. Due to the limitations of hot-wire probes in measuring low velocities, in this case close to the boundary-layer edge, we chose to calculate the integral parameters using δ_{95}^* instead of integrating across the whole boundary layer, such that the displacement thickness $\delta_{1,95}^*$ is

$$\delta_{1,95}^* = \int_0^{\delta_{95}^*} \frac{V^*(z^*)}{V_w^*} \mathrm{d}z^*. \tag{2.1}$$

For the same reason, the momentum thickness $\delta_{2,95}^*$ is defined as

$$\delta_{2,95}^* = \int_0^{\delta_{95}^*} \left(1 - \frac{V^*(z^*)}{V_w^*}\right) \frac{V^*(z^*)}{V_w^*} \mathrm{d}z^*. \tag{2.2}$$

The shape factor H_{95} is defined as $H_{95} = \delta_{1,95}^*/\delta_{2,95}^*$ and the theoretical value using the similarity profile is 2.23. The theoretical shape factor based on the full boundary-layer thickness gives 2.12 instead. As can be seen from table 1 excellent agreement with the theoretical value for laminar flow is obtained up to $R = 530$.

Case	R	R_{edge}	r^* (mm)	Ω^* (r.p.m.)	z	δ_{95}	δ_{95}^* (mm)	$\delta_{1,95}^*$ (mm)	$\delta_{2,95}^*$ (mm)	H_{95}
PP01	410	488	198	628	0.4–16	3.65	1.76	0.587	0.263	2.23
PP02	430	512	198	690	0.4–16	3.61	1.66	0.557	0.249	2.24
PP03	450	535	198	755	0.4–16	3.61	1.59	0.533	0.239	2.23
PP04	470	559	198	822	0.4–16	3.62	1.52	0.512	0.229	2.23
PP05	490	583	198	890	0.4–16	3.63	1.47	0.494	0.220	2.24
PP06	510	606	198	963	0.4–16	3.61	1.40	0.474	0.211	2.25
PP07	530	630	198	1040	0.4–16	3.57	1.34	0.456	0.203	2.25
PP08	550	654	198	1122	0.4–16	3.69	1.33	0.453	0.207	2.18
PP09	570	677	198	1205	0.4–16	4.77	1.66	0.488	0.246	1.99
PP10	590	702	198	1295	0.4–26	8.78	2.94	0.632	0.401	1.58
PP11	610	725	198	1385	0.4–26	12.1	3.94	0.767	0.531	1.46
PP12	630	749	198	1480	0.4–26	14.4	4.52	0.848	0.600	1.41
IP01	360–605	618	137–231	1000	1.3	—	—	—	—	—
IP02	360–700	731	116–226	1400	1.3	—	—	—	—	—

TABLE 1. Experimental conditions. Here, r^* is the local radius of the hot-wire probe, Ω^* the rotational speed, z the normalized wall-normal position, δ_{95} the normalized boundary-layer thickness $(\delta_{95} = \delta_{95}^*(\Omega^*/\nu^*)^{1/2})$, where δ_{95}^* is defined as the wall-normal height where the azimuthal velocity is 5 % of the disk velocity, $\delta_{1,95}^*$ the displacement thickness, $\delta_{2,95}^*$ the momentum thickness and $H_{95} = \delta_{1,95}^*/\delta_{2,95}^*$ the shape factor.

3. Results

3.1. *Azimuthal mean velocity profiles*

The azimuthal mean velocity profiles at various Reynolds numbers are shown in figure 2(*a*). At low Reynolds number the measured data are in accordance with the theoretical laminar profile as well as the theoretical boundary-layer thickness. Figure 2(*b*) shows the deviation of the azimuthal mean velocity profiles from the theoretical laminar profile. The deviation from the theoretical profile can be observed at $R = 550$. Local linear stability analysis (Lingwood 1995, 1997*a*) showed that local absolute instability occurs above $R = 507$ and that the absolute instability may trigger nonlinearity. Imayama *et al.* (2013), using the same data as the present study, observed the rise of the first harmonic in the spectra at $R = 510$, indicating the onset of nonlinearity, and observed that this R-value was highly reproducible under various experimental conditions. Distortion of the mean velocity profile is known not to be a sensitive detector of the onset of nonlinearity (e.g. see the reinterpretation in Imayama *et al.* 2013 of the transition Reynolds number given by Othman & Corke 2006 originally based on mean-flow deformation) and therefore it is not surprising that the start of observable deviation in the mean profile is not seen until higher values of about $R = 550$. Once the deviation of the profiles starts around $R = 550$, the shape of the velocity profile changes considerably over a small range of R, resulting in a thicker boundary layer and a steeper velocity gradient close to the wall, and for high enough R the boundary layer is seen to be fully turbulent. Imayama *et al.* (2012) suggested for similar conditions as the present experiments that the fully developed turbulent boundary layer is observed above $R = 650$.

Figure 3 shows azimuthal mean velocity measurements as functions of Reynolds number in a log–logplot (see also table 1). One of the characteristics of the rotating-disk boundary-layer flow is that the dimensional boundary-layer thickness,
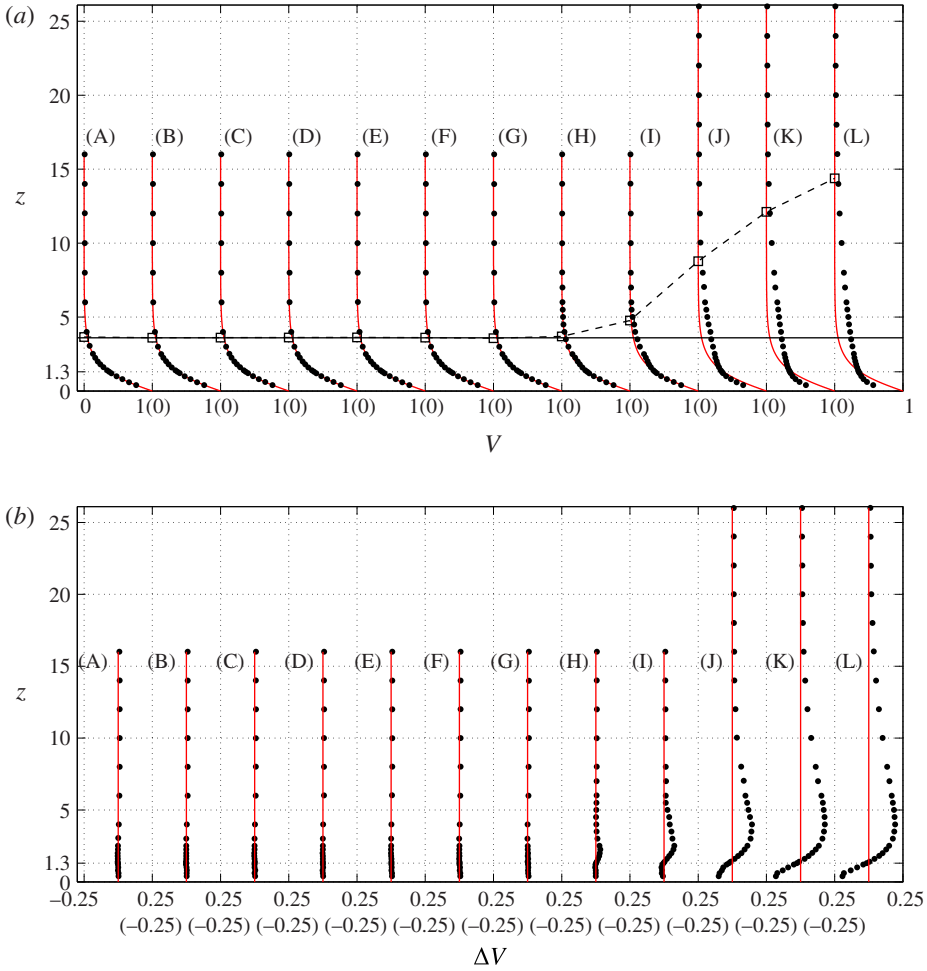
FIGURE 2. (Colour online) (*a*) Azimuthal mean velocity, *V*, profiles and (*b*) azimuthal mean velocity deviation from the theoretical laminar profile, ΔV. Profiles measured for cases PP01–12 at (A) $R = 410$, (B) $R = 430$, (C) $R = 450$, (D) $R = 470$, (E) $R = 490$, (F) $R = 510$, (G) $R = 530$, (H) $R = 550$, (I) $R = 570$, (J) $R = 590$, (K) $R = 610$, (L) $R = 630$. The solid lines at each Reynolds number show the theoretical azimuthal laminar velocity profiles. The solid line at $z = 3.60$ indicates the normalized theoretical boundary-layer thickness for the laminar profile where *V* becomes 0.05. The squares with the dashed line show the measured boundary-layer thickness (δ_{95}) given in table 1.

displacement thickness and momentum thickness in the laminar region are constant with varying radius (Reynolds numbers) at a constant rotational speed. However, for the PP01–12 cases in table 1 the radius is fixed, and the Reynolds number is increased by increasing the rotational speed, which gives a decreasing boundary-layer thickness. The non-dimensional boundary-layer thickness is given as $\delta = \delta^*\sqrt{\Omega^*/\nu^*}$ giving

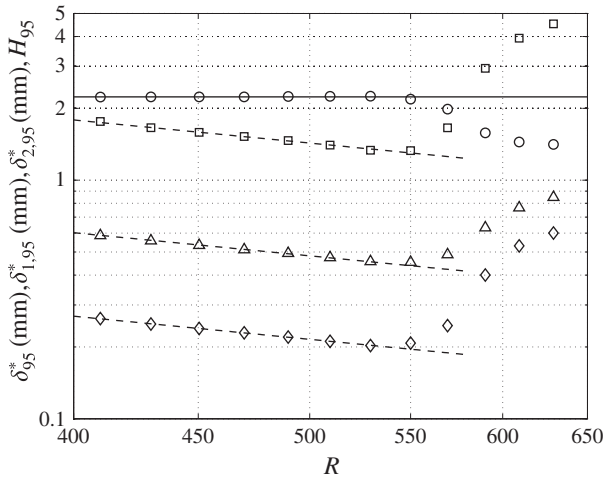$$\delta^* = \delta\sqrt{\frac{\nu^*}{\Omega^*}} = \delta\frac{r^*}{R}. \tag{3.1}$$

FIGURE 3. The rotating-disk boundary-layer characteristics as functions of Reynolds number in log–log scale: □, the boundary-layer thickness, δ_{95}^*; △, the displacement thickness, $\delta_{1,95}^*$; ◇, the momentum thickness, $\delta_{2,95}^*$; ○, the shape factor, H_{95}. The solid line shows the theoretical shape factor, $H_{95} = 2.23$, based on the boundary-layer thickness δ_{95}^*. The dashed lines indicate slopes of -1.

Hence, in the laminar region a log–log plot of the boundary-layer thickness versus R should show a slope of -1. Figure 3 shows the data together with fitted lines with slope -1 giving good agreement. The boundary-layer thicknesses all start to deviate from the theoretical line around $R = 550$, which is again an indication that this is where the laminar profile starts to be deformed due to nonlinearity, as shown in figure 2. At the same position the shape factor starts to decrease and reaches 1.41 at $R = 630$, close to what is expected for a turbulent boundary layer at low Reynolds numbers and is in good agreement with the experimental results of Cham & Head (1969), see their figure 5.

3.2. *Velocity-disturbance characteristics*

The root-mean-square (r.m.s.), skewness and flatness variation with Reynolds number obtained at a constant height $z = 1.3$ are reported in figure 4(a,c,d). The z-position was chosen to coincide with the maximum measured amplitude of the stationary vortices in the laminar region, which is shown in § 3.4.

The velocity data were obtained in two different ways. First (PP01–12, see table 1), the rotational speed was varied, keeping the hot-wire probe at a constant radial position, and the data at $z = 1.3$ were extracted from measurements used for the mean velocity distributions reported in figure 2. Secondly (IP01–02), the radial position of the probe was varied keeping a constant rotational speed and the non-dimensional wall-normal position was kept constant at $z = 1.3$. Here, the measurements were taken at intervals of $\Delta R = 5$. For these measurements the edge Reynolds numbers vary; however Imayama *et al.* (2013) showed that this does not affect the instability and transition process significantly.

Figure 4(a) shows $v_{rms}(= v_{rms}^*/r^*\Omega^*)$ distributions where the filled symbols are results obtained directly from the hot-wire anemometer signal. At low Reynolds number, the IP02 case shows the highest background noise level compared with the
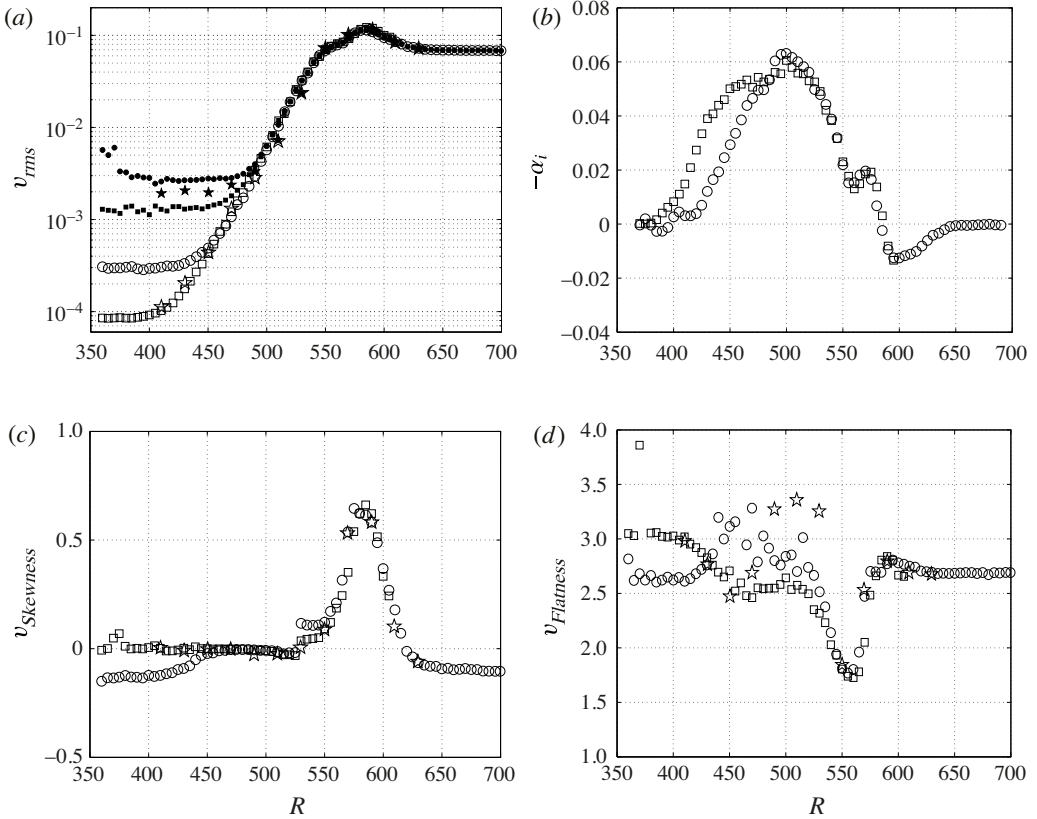
FIGURE 4. (*a*) Azimuthal fluctuation velocity v_{rms}, (*b*) growth rates α_i, (*c*) skewness, and (*d*) flatness distributions, measured at $z = 1.3$. The symbols indicate cases: ☆, PP01–12; □, IP01; ○, IP02. The filled symbols denote unfiltered data, the unfilled symbols show band-pass filtered data ($17 < \omega^*/\Omega^* < 70$) below $R \leqslant 490$ and high-pass filtered signal ($17 < \omega^*/\Omega^*$) for $495 \leqslant R \leqslant 525$, where ω^* is the frequency measured in the laboratory frame.

other cases. This is due to the much higher rotational speed in that case, which causes low-frequency vibration of the system. The PP01–04 cases also have higher disturbance amplitudes compared with the IP01 case for low R despite lower rotational speeds. This is probably because the effect of any rotational imbalance is greater at larger radius. To maximize the signal-to-noise ratio (noise typically being vibration and imbalance at low frequencies and electronic noise at high frequencies) in the measured time series, the signals were filtered with a band-pass filter $17 < \omega^*/\Omega^* < 70$ below $R \leqslant 490$ and with a high-pass filter $17 < \omega^*/\Omega^*$ for $495 \leqslant R \leqslant 525$, where ω^* is the signal frequency. At higher Reynolds numbers, the disturbance amplitudes become so large that the background noise becomes negligible in comparison without filtering.

The resulting filtered r.m.s.-distributions are shown as unfilled symbols in figure 4(*a*). The filtered data show exponential disturbance growth from lower Reynolds numbers than the unfiltered data but, even with filtering, the background noise cannot be removed completely at very low Reynolds number. Linear stability analysis (e.g. Malik *et al.* 1981) shows the onset of growth of the stationary mode

from about $R = 290$ and for the travelling mode the critical Reynolds number is even lower than for the stationary mode. In figure 4(*b–d*) only filtered data are shown.

Figure 4(*a*) shows excellent agreement for the different measurement conditions of the IP01, IP02 and PP cases except for $R \leqslant 450$ where the background noise levels control the differences observed. Exponential growth of v_{rms} is observed up to $R = 550$ beyond which the v_{rms} amplitude continues to increase (to $R = 585$) but with a slower rate. Above $R = 550$, deviation of the azimuthal mean velocity profile from the theoretical laminar profile starts, as shown in figure 2(*b*). Thus, it is expected that nonlinearity would be active at these Reynolds numbers. At $R = 585$ where the maximum v_{rms} is observed, figure 2(curves I, J) show rapid growth of the boundary-layer thickness, indicating turbulent breakdown. For $R > 650$ the disturbance amplitude becomes almost constant indicating that the boundary layer has become fully turbulent.

From the amplitudes of v_{rms} it is possible to calculate the radial growth rate $-\alpha_i$, assuming that $v_{rms} \sim \exp(-\alpha_i R)$, as is presented in figure 4(*b*). The growth rate is obtained by fitting a line through five neighbouring points (using a least-squares fit), i.e. the fitting points are taken over a range of $\Delta R = 20$. In figure 4(*b*), $-\alpha_i$ is taken as the radial spatial growth of the total disturbance amplitude, i.e. both stationary and unsteady disturbances, as represented in figure 4(*a*).

One should be aware that the dimensional growth of the disturbance is larger than that obtained from the slope in figure 4(*a*) due to the normalization of v_{rms}^* by V_w^*, which increases with Reynolds number. To clarify this, we can express the normalization in the following form:

$$\frac{v_{rms}^*}{V_w^*} = R^{-2} \frac{v_{rms}^* r^*}{v^*}.$$

As an example, for our configuration, if the Reynolds number is changed from 500 to 550 by increasing the rotation speed, then the normalizing velocity increases with a factor of 1.21 whereas if the Reynolds number is changed the same amount by increasing the radius the normalization velocity increases with a factor of 1.10. In a local theoretical analysis this is of no concern but it will influence the growth rate obtained from data such as shown in figure 4(*a*) (albeit a small effect in relation to the values of $-\alpha_i$) and would complicate comparison of data from cases PP01–12 (with varying rotational speed) with cases IP01-02 (with varying radius). In any case, the PP01–12 cases are not shown in figure 4(*b*) due to too few data points for an accurate determination of the growth rate.

In figure 4(*b*), the IP01 and IP02 cases differ for $400 \leqslant R \leqslant 475$ because of the different background noise levels in the two cases, as shown in figure 4(*a*). However, the growth rate has a distinct maximum value at around $R = 500$ and starts decreasing above this Reynolds number. This decrease in the growth rate can be explained by the appearance of nonlinearity and these plots suggest that the radial growth rate can act as a good indicator of the onset of nonlinearity. The local absolute instability appears above $R = 507$, which is likely to trigger the nonlinearity and this is supported by the highly repeatable appearance of the onset of nonlinearity in the range $510 \leqslant R \leqslant 520$ under various measurement conditions shown by Imayama *et al.* (2013).

Figure 4(*c,d*) shows the skewness and flatness of the azimuthal fluctuating velocity (calculated from the same data and with the same filtering as in figure 4*a*). The skewness and flatness are defined as

$$v_{Skewness} = \frac{\overline{v^3}}{v_{rms}^3} \quad \text{and} \quad v_{Flatness} = \frac{\overline{v^4}}{v_{rms}^4},$$

respectively. The bar over the azimuthal fluctuation velocity, v, indicates the mean of the value. The skewness plotted in figure 4(*c*) shows good agreement between the different measurement conditions except for $R < 450$ due to the differing background noise levels. Le Gal (1992) performed rotating-disk flow experiments in a water-filled container using a hot-film probe and proposed that the sudden change in the variation of the second- and third-order moments occurs simultaneously and that they are good indicators of the transition to turbulence. In figure 4(*c*) the most skewed behaviour is observed around $R = 585$ and the peak of v_{rms} is observed at the same Reynolds number, where figure 2(*a*) also shows thickening of the boundary layer. Our results correspond to those of Le Gal (1992), and according to these indicators and using his transition definition the transition Reynolds number would be $\sim$585. Furthermore, Imayama *et al.* (2012) proposed a new way to describe transition characteristics of a rotating-disk flow by utilizing the Reynolds number variation of the probability density function (p.d.f.) as an indicator of transition. A similar approach was also taken in Le Gal (1992). However, the p.d.f. map given by Imayama *et al.* (2012) captures the characteristics of the transition process much more visually and clearly. The application of the p.d.f. map to the wall-normal profile can be used to reveal the wall-normal structure of the primary vortices and the vertical structure associated with secondary instability at $R = 570$, see figure 7 in Imayama *et al.* (2012). The skewness is sensitive to the tail shape of the p.d.f. and the peak in figure 4(*c*) at about $R = 585$ corresponds to the positive expansion of the p.d.f. in figure 6 of Imayama *et al.* (2012), which is calculated from the same data as described here as IP02.

As expected for higher moments, the flatness distribution in figure 4(*d*) has more scatter for the different cases than the quantities shown in figure 4(*a*–*c*). For a signal with a Gaussian distribution the flatness has a value of 3. At the lower Reynolds numbers, the single-realization time series have amplitude modulation due to inhomogeneously distributed initial disturbances hence the flatness is close to but not exactly as expected for a Gaussian distribution. For $R > 510$ the disturbance amplitude has grown sufficiently for the flatness to decrease and it has a minimum at about $R = 550$, which is a little upstream from the peaks in disturbance amplitude and skewness shown in figures 4(*a*) and 4(*c*). This behaviour shows that the amplitude modulation of the single-realization time series reduces over this Reynolds number range and the flatness becomes close to 1.5, which is the value expected of a sinusoidal signal without amplitude modulation. These characteristics are also seen in §3.5 in the time series. Above $R = 550$ and the minimum in flatness, the single-realization time series become skewed; see the positive skewness in figure 4(*c*). Finally, $v_{Flatness} \approx 2.7$ at $R > 635$, which is within the range observed in turbulent boundary-layer flows within the buffer and log regions; see, for example, figure 2(*j*) in Imayama, Lingwood & Alfredsson (2014).

3.3. *Velocity-disturbance spectra*

To visualize frequency information, power spectra, $P(\omega^*)$, of single-realization time series are plotted in figure 5 at intervals of $\Delta R = 5$ between $R = 500$ and $R = 650$ measured at $z = 1.3$. (The same definition of $P(\omega^*)$ is used here as in Imayama *et al.* 2013.) The spectra are obtained from time series containing $\sim$1 million points, where the sampling rate is 720 samples per disk revolution. The time series are divided into 492 segments of 2048 data points each and the 492 spectra are averaged. However, as will be shown later the modulation of the stationary vortices gives rise to spiked spectra and, in order to smooth the spectra, a moving average is applied to $P(\omega^*)$. The
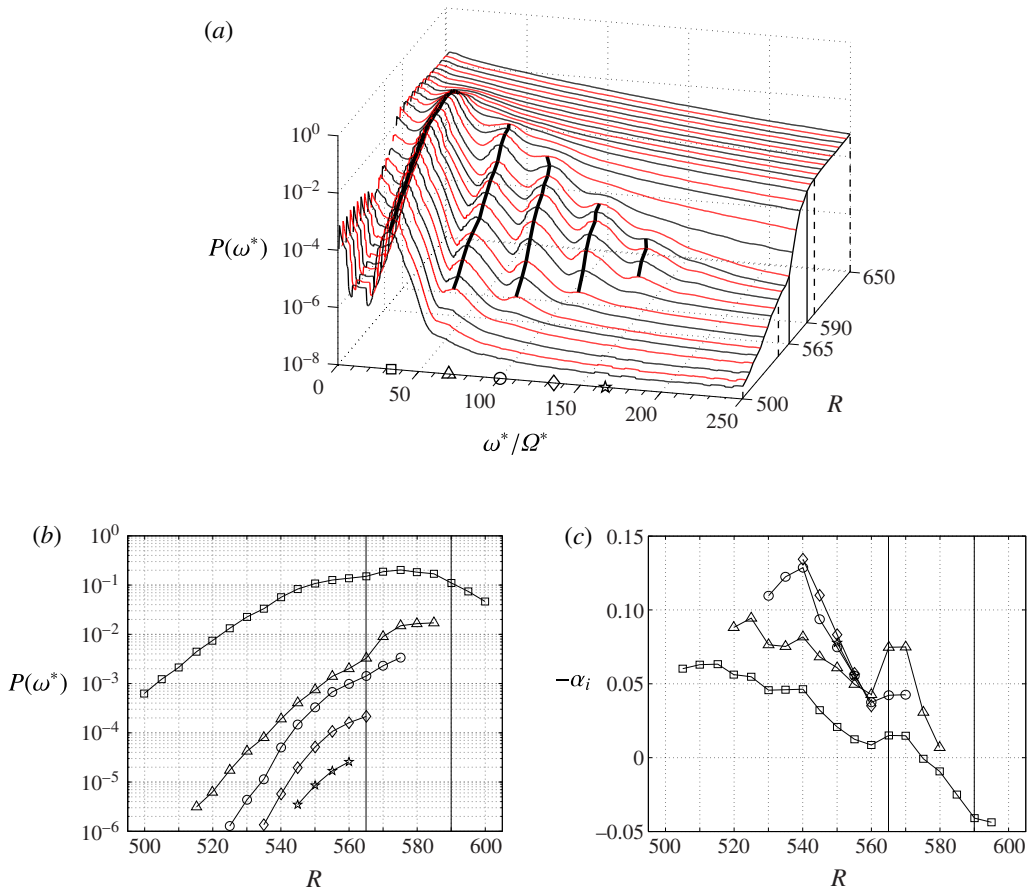
FIGURE 5. (Colour online) Spectra measured at $z = 1.3$ (IP02). (*a*) Spectra with moving average $P(\omega^*)$ at $\Delta R = 5$ intervals between $R = 500$ and 650. $R = 500, 550, 600, 650$ are indicated by dashed lines. The thick solid lines link the peaks of the primary and harmonics in the spectra. The symbols located on the *x*-axis indicate the averaged frequencies of the thick solid lines: $\square$, primary; $\triangle$, first harmonic; $\bigcirc$, second harmonic; $\diamond$, third harmonic; $\star$, fourth harmonic, respectively. Vertical solid lines at $R = 565, 590$ indicate the region of rapid growth of high-frequency components. These solid lines are also shown in (*b* and *c*). (*b*) The amplitude distribution of the primary and harmonic spectra indicated in (*a*). (*c*) The exponential radial growth rate of the primary and harmonics. The symbols in (*b*) and (*c*) are the same as in (*a*).

moving average is of box type with 25 points corresponding to a window of $\omega^*/\Omega^* \approx$ 8. The details of the spikes will be discussed later in the Appendix. The spectra in figure 5 are calculated using the IP02 data, i.e. measured with a fixed rotation speed with the Reynolds number increased by increasing the radial measurement position.

At $R = 500$ the primary spectral peak is observed around $\omega^*/\Omega^* = 30$ as reported by many experimental studies (Gregory *et al.* 1955; Kobayashi *et al.* 1980; Kohama 1984; Wilkinson & Malik 1985; Jarre, Le Gal & Chauve 1996; Lingwood 1996; Othman & Corke 2006; Imayama *et al.* 2012, 2013; Harris *et al.* 2012) and is due to the primary vortices (stationary in the rotating frame) passing the hot-wire probe. The peak at $\omega^*/\Omega^* = 1$ is due to the small rotational imbalance of the disk and,

as shown, does not change amplitude with R. The first harmonics of the primary instability can be seen in figure 5(*a*) to appear around $R = 510$ and the number of harmonics increases as the Reynolds number increases indicating the strengthening of the nonlinearity, corresponding to the reduction in the radial growth rate of the primary instability above $R = 510$, as observed in figure 4(*b*).

Figure 5(*a*) gives a clear impression of the filling out of the high-frequency region at $R = 565$–590, indicating turbulent breakdown over this range of the Reynolds number. Since each power spectrum is constructed from a time series measured over several rotations of the disk, this does not give information about any azimuthal variation in the turbulent-breakdown behaviour at a given radius (or Reynolds number). We consider azimuthal variation later but here this result shows that the transition process is to a large extent dictated by the value of the Reynolds number. A recent numerical study by Viaud *et al.* (2011) similarly captures this rapid turbulent breakdown. They performed a direct numerical simulation in an open rotating cavity showing transition to turbulence through a steep-nonlinear global mode with a secondary global mode leading to 'a very disorganized state'. They suggested that the appearance of the secondary instability and the disorganized state sitting a little downstream of the primary global front constituted a 'secondary front' (based on the spectrum in their figure 5). Comparing their figure 5 with the projection on the right-hand side of figure 5(*a*) here, the rapid development of high-frequency components at $R = 565$–590 seems to correspond to their result. However, the spectra in figure 5(*a*) do not capture obvious signs of secondary instability in this region. Detailed attention is given to secondary instabilities in § 3.5.

Imayama *et al.* (2012) suggested that the change of the slope in v_{rms} as a function of R around $R = 545$ in their figure 5 could correspond to Viaud *et al.*'s (2011) 'secondary front'. However, the present spectrum shows that if the secondary front exists it is more likely to lie at a higher value, e.g. $R = 565$–590. This Reynolds number corresponds to the peak of v_{rms} and $v_{Skewness}$ in figure 4(*a*,*c*) and rapid growth of boundary-layer thickness in figure 2(curves I, J). The reason for the change of the slope in v_{rms} at around $R = 545$–550 in figure 4(*a*) is discussed in § 3.4.

Peak amplitudes of the primary frequency and its harmonics are shown in figure 5(*b*). The peak frequency positions are shown as thick solid lines in figure 5(*a*). The peak amplitude of the primary frequency increases with Reynolds number up to $R = 550$; however at $R = 550$ the growth becomes almost saturated and the amplitude starts to decrease above $R = 585$ indicating turbulent breakdown of the primary vortices. The peak amplitudes of the harmonics have steeper growth than the primary instability. The growth rates of the peak amplitudes of the primary frequency and its harmonics are presented in figure 5(*c*), where the relation is given as $\sqrt{P(\omega^*)} \sim \exp(-\alpha_i R)$. The growth rates of the harmonics appear to collapse onto common values for $R = 550$–560, where the change in the slope in v_{rms} is observed in figure 4(*a*).

Local stability analysis shows that the rotating-disk flow has stationary unstable waves and also travelling unstable waves, see for example figure 6 in Lingwood (1995). Here, we have shown the total (or combined) spectral characteristics of the flow in figure 5, without distinguishing between the frequency contributions from stationary and travelling modes. Note, that if spectra are calculated from ensemble-averaged time series (as opposed to averaging the spectra of single-realization time series, as here) then only the repeatable, continuously excited stationary waves are retained in the spectra (see, for example, figure 15 in the Appendix). As discussed in the Introduction (§ 1), the travelling disturbances are often overlooked because the stationary disturbances are more easily observed and measured.

For a stationary mode the normalized frequency, ω^*/Ω^*, detected by the hot-wire probe in the laboratory frame directly corresponds to the integer azimuthal wavenumber, β. However, a travelling mode with non-zero frequency $\omega_t^* = \omega_c R\Omega^*$, in the rotating frame, and azimuthal wavenumber, β, is observed at a frequency $\omega^*/\Omega^* = \omega_t^*/\Omega^* + \beta$ in the laboratory frame of reference, where ω_c is the non-dimensional frequency corresponding to that obtained from local linear stability analysis in a rotating frame. A single hot-wire probe fixed in the laboratory frame gives ω^* but cannot give the frequency ω_t and azimuthal wavenumber separately. Therefore, it is difficult to distinguish stationary from travelling disturbances, especially if the measured frequencies are similar, resulting in merging of the modes in the spectra. Nevertheless, we show in figure 6(*a–f*) that it is possible to distinguish these modes.

Figure 6(*a–f*) shows high-resolution power spectra, $P(\omega^*)$, at intervals of $\Delta R = 20$ between $R = 410$ and $R = 630$ and at different wall-normal positions. In contrast to figure 5(*a*) the power spectra in figure 6(*a–f*) are shown without any smoothing, which helps to distinguish stationary from travelling modes. Figure 6(*b*) shows data measured at the same wall-normal height as figure 5. In the unstable and turbulent-breakdown regions at $R = 410$–610, there are two notable characteristics shown by the spectra. First, without the smoothing of figure 5(*a*), the spectra have regions with regular spikes at integer values of ω^*/Ω^* and, secondly, a relatively smooth peaked region on the downward slope of the primary and its harmonics; see particularly figure 6(*e,f*) measured at the higher wall-normal heights at $\omega^*/\Omega^* \approx 40$, which helps to identify this feature in the other subplots of figure 6. As mentioned in the previous section (and see the Appendix), the integer spikes are due to the modulation of the stationary disturbance. We suggest here and show in figure 15 (see Appendix) that the smooth spectral hump at $\omega^*/\Omega^* \approx 40$ is due to travelling disturbances.

Below the onset of absolute instability one might expect the most convectively unstable travelling modes to determine the travelling spectral peak. At $R = 507$, the nonlinear global mode might be expected to give the critical azimuthal wavenumber and frequency of the local absolute instability, which are $\beta = 68$ and $\omega_c = -0.0349$, respectively, see table 3 in Lingwood (1997*a*). Such waves would give an observed frequency in the laboratory frame of $\omega^*/\Omega^* = -0.0349 \times 507.3 + 68 = 50.3$. However, as with figure 9 in Lingwood (1996), here we show that the travelling components are centred around $\omega^*/\Omega^* \approx 40$ above about $R = 500$ and so figure 6 does not clearly capture the local absolute frequency predicted theoretically. Nevertheless, this perhaps corresponds to the global mode realized in the physical flow, which has a more complex base flow than accounted for in theoretical analyses due, for example, to unavoidable convectively unstable stationary vortices. A stability analysis of the azimuthally varying base flow would clarify the effects on the absolute instability and global stability characteristics but this lies outside the scope of this experimental investigation.

3.4. *Stationary and unsteady velocity-disturbance amplitudes*

In figure 6 differences in the spectral characteristics of travelling and stationary modes were shown. In this section, we investigate the different characteristics of the disturbance field by decomposing the velocity fluctuations into stationary and unsteady contributions.

The procedure for decomposition is as follows. The hot-wire measurements are taken with reference to an angular datum. This makes it possible to ensemble average the velocity time series for individual rotations of the disk, giving the part
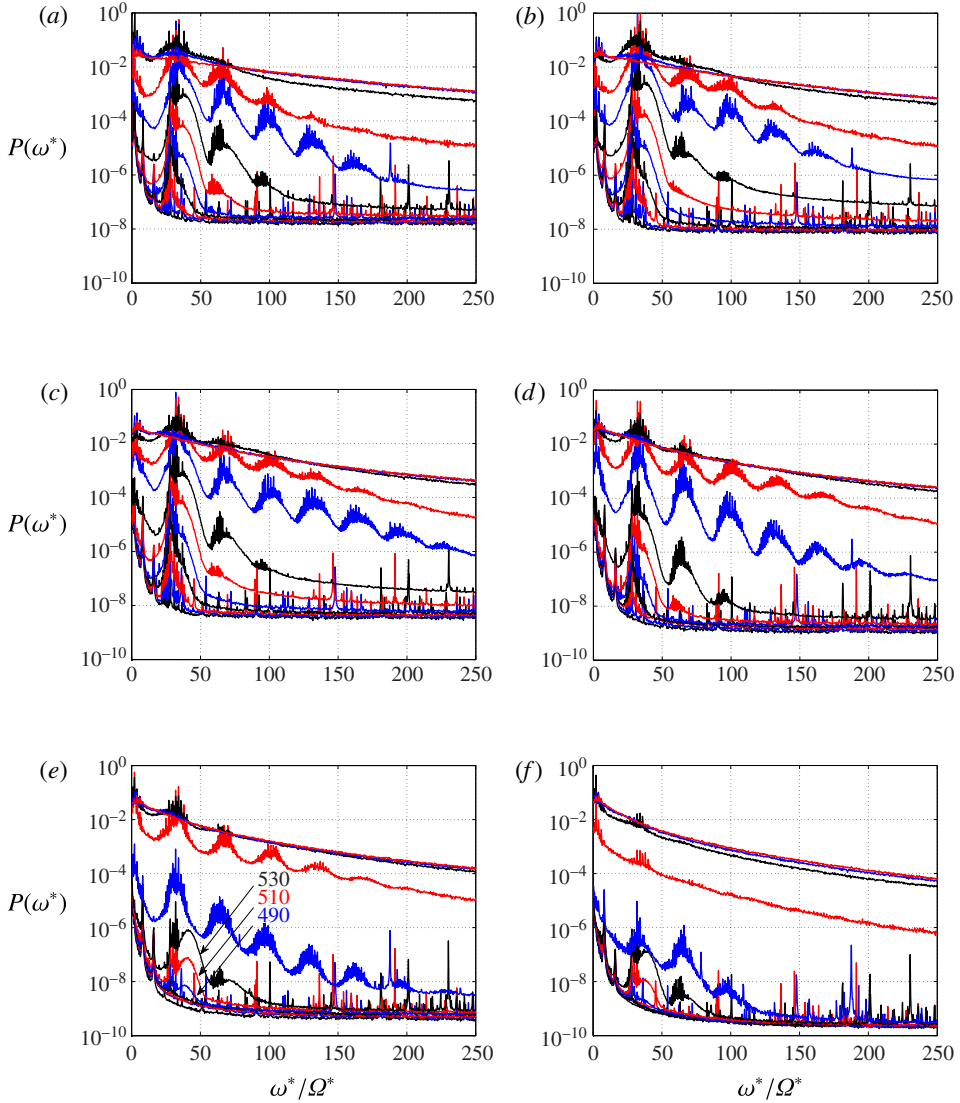
FIGURE 6. Spectra measured at (*a*) $z = 0.6$, (*b*) $z = 1.3$, (*c*) $z = 2.0$, (*d*) $z = 3.0$, (*e*) $z = 4.0$, (*f*) $z = 6.0$. The spectra are shown in black, blue and red repeatedly in that order between $R = 410$ and $R = 630$ at $\Delta R = 20$ intervals.

of the time series, $v_{rms,st}$, corresponding to the stationary modes. The time series for the remaining unsteady part, $v_{rms,us}$, is calculated from the total disturbance and stationary disturbance fields as follows (under the assumption that the stationary and the unsteady parts are uncorrelated, which is justified by calculations that show a correlation of less than a maximum of 1 %):

$$v_{rms,us} = \sqrt{v_{rms}^2 - v_{rms,st}^2}.$$

The unsteady disturbances are a combination of noise (particularly at low Reynolds numbers), travelling waves, time variation of the stationary disturbance field and, at
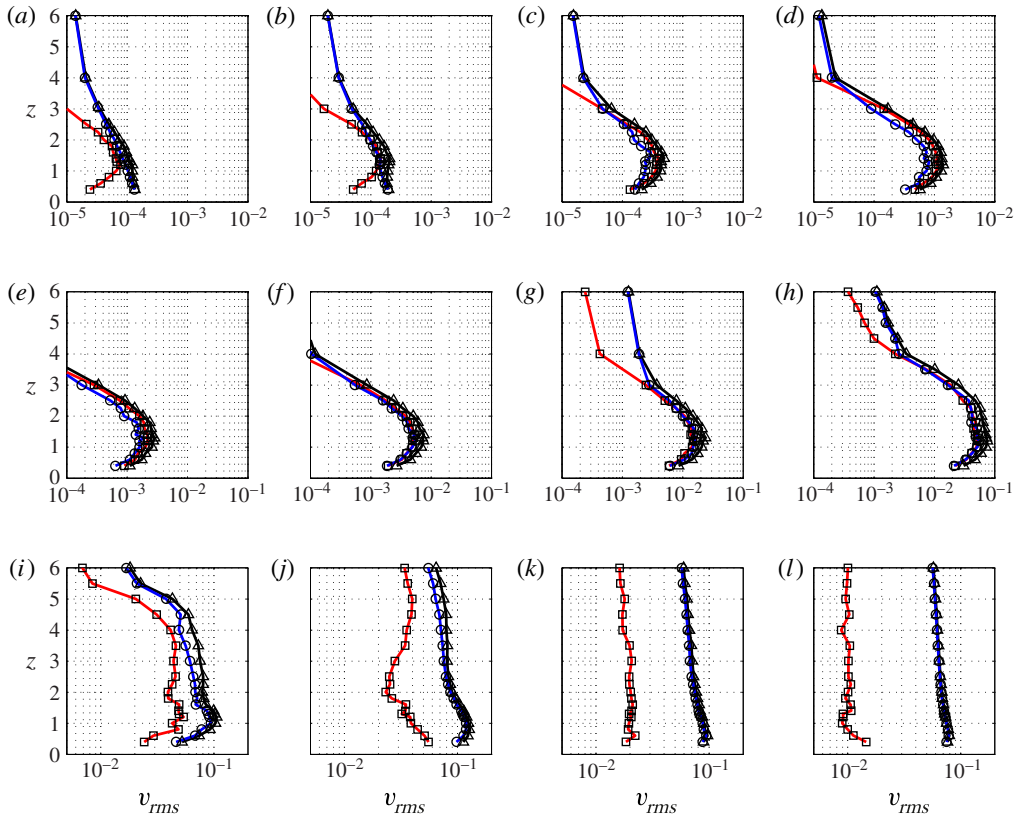
FIGURE 7. (Colour online) Profiles of the azimuthal fluctuating velocity amplitude measured at (*a*) $R = 410$, (*b*) $R = 430$, (*c*) $R = 450$, (*d*) $R = 470$, (*e*) $R = 490$, (*f*) $R = 510$, (*g*) $R = 530$, (*h*) $R = 550$, (*i*) $R = 570$, (*j*) $R = 590$, (*k*) $R = 610$, (*l*) $R = 630$. The symbols indicate: $\triangle$, total velocity disturbance amplitude, v_{rms}; $\bigcirc$, unsteady velocity disturbance amplitude, $v_{rms,us}$; $\square$, stationary velocity disturbance amplitude, $v_{rms,st}$, respectively. Filtered data are shown at $R = 410$–510 in the same manner as figure 4(*a*).

high Reynolds numbers, unsteady turbulent fluctuations. Figure 7 shows disturbance amplitude profiles of the total, the stationary and the unsteady components at intervals of $\Delta R = 20$ in the range $R = 410$–630.

The velocity-disturbance profiles for the stationary component in figure 7(*a*) show a maximum at about $z = 1.3$. For the unsteady component the maximum amplitude is observed close to the wall and it does not change between $R = 410$ and 430 indicating that the unsteady disturbance is dominated by background noise rather than a physical instability. However, by $R = 450$, the unsteady disturbance amplitude starts to increase and at $R = 470$ (figure 7*d*) a peak is clearly observed, also around $z = 1.3$. These two types of disturbances grow with increasing Reynolds number with almost the same growth rate and maximum peak position up to $R = 530$. However, at $R = 550$ (figure 7*h*), the disturbance profile starts to grow in the wall-normal direction, as does the mean velocity profile shown in figure 2(*a*).

At $R = 570$ an obvious difference between the stationary and unsteady disturbances can be seen. The unsteady disturbance profile has much higher amplitude than the stationary one in figure 7(*i*). The stationary disturbance profile has a second peak

around $z = 3.0$–3.5 in addition to the first peak around $z = 1.3$. Furthermore, the amplitude of $v_{rms,st}$ at $z = 1.3$ does not grow significantly between $R = 550$ and $R = 570$, possibly because of nonlinear saturation of the stationary mode (see below). Meanwhile, the unsteady disturbance continues growing with the maximum peak moving closer to the wall than $z = 1.3$. The total disturbance amplitude is mostly due to the unsteady disturbance around $z = 1.3$. By $R = 590$, the amplitude of the stationary disturbance has decreased compared with $R = 570$, possibly as a result of turbulent breakdown of the stationary mode; the contribution of the unsteady disturbance to the total disturbance amplitude is dominant. At $R = 610$–630 (figure 7*k,l*) the total disturbance amplitude is almost entirely composed of unsteady disturbances due to the almost fully turbulent nature of the boundary layer.

The decomposition of v_{rms} into stationary and unsteady disturbance fields is also applied to the disturbance growth measurements at constant wall-normal height, namely to the IP01 and IP02 cases, as shown in figure 8. The total disturbance amplitude for these two cases shows good agreement with figure 4(*a*) except at low Reynolds numbers due to different background noise levels. In figure 8(*a,b*) exponential growth of stationary disturbances is observed at $R = 360$–550. In good agreement with figure 4(*b*), figure 8(*c,d*) shows the growth rate of the stationary disturbances increasing with Reynolds number and approaching $-\alpha_i \approx 0.06$ at $R = 500$. Hussain *et al.* (2011) showed a linear convective growth rate for the stationary mode in their figure 6, which is in accordance with the present results. For $R > 500$, figure 8(*c,d*) show the growth rate of the stationary disturbance decreasing, presumably due to nonlinear effects as shown in figure 5(*a*). Furthermore, around $R = 550$ the stationary mode becomes saturated and its amplitude starts to decrease at $R = 570$–580, indicating turbulent breakdown. This saturation in growth of the stationary disturbances causes the change in the slope with increasing R at $R = 550$ in total disturbance amplitude, v_{rms}.

Meanwhile, the growth of the unsteady disturbances behaves differently from the stationary disturbances particularly in the later stage of the transition process. At low Reynolds number, the total disturbance amplitude is dominated by unsteady background noise. Above $R \approx 450$, the travelling disturbances start increasing exponentially and form the major part of the unsteady disturbance field, and, similar to the stationary disturbances, the growth rate of the unsteady components also decreases above $R = 500$–510. However, in contrast to the stationary mode, the unsteady disturbance amplitude continues to increase above $R = 550$ up to $R = 585$, such that between these Reynolds numbers the total disturbance amplitude is dominated by the unsteady component.

The chain lines in figure 8 indicate the Reynolds number for the onset of the absolute instability obtained from local stability analysis. Global behaviour (i.e. accounting for spatial inhomogeneity) of the rotating-disk flow has been discussed in early studies. Although Davies & Carpenter (2003) numerically demonstrated that the rotating-disk flow does not exhibit global instability in the linear approximation despite absolute instability existing in the semi-infinite region beyond the critical Reynolds number, Healey (2010) has recently shown using a model equation, taking into account the finite nature of a disk, that the local absolute instability gives rise to linear global instability resulting directly in a primary nonlinear steep-fronted global mode. Figure 8(*c,d*) shows that at $R = 507$ the radial growth rate starts to decrease presumably due to the nonlinear effects. Building on Pier's (2003) nonlinear approach, which suggested that the flow has a primary nonlinear global mode (a so-called 'elephant mode', see Pier & Huerre 2001; Chomaz 2005) fixed at the onset
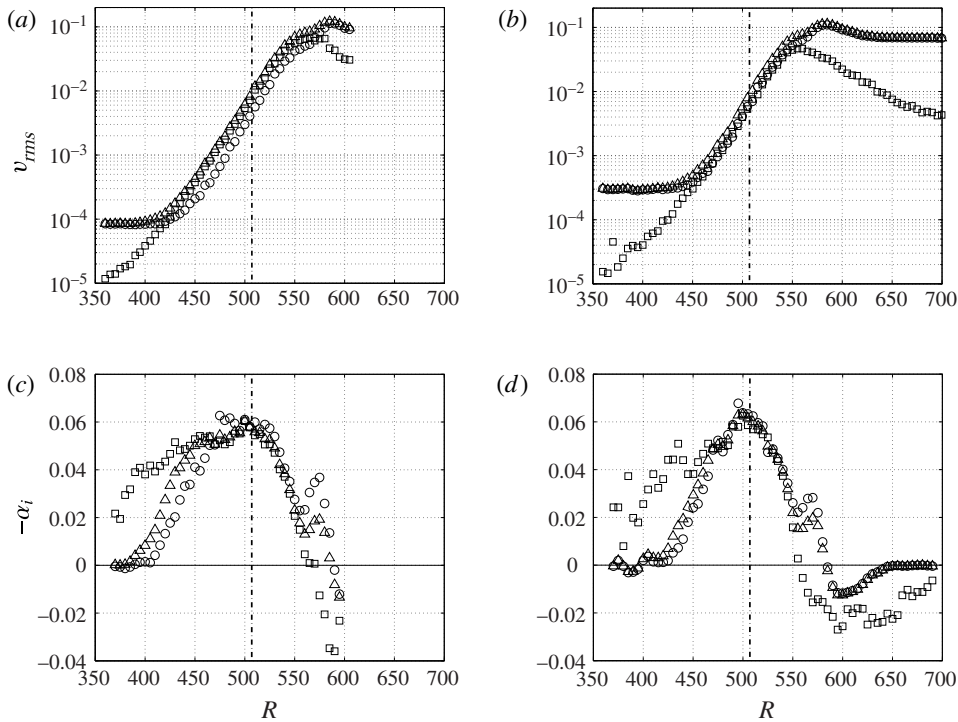
FIGURE 8. (*a,b*) The v_{rms} ($\triangle$), $v_{rms,st}$ ($\square$), $v_{rms,us}$ ($\bigcirc$) distributions measured at $z = 1.3$ with two edge Reynolds numbers, $R_{edge} = 618, 731$ (IP01, IP02) cases, respectively. (*c,d*) The growth rate of the total disturbance ($\triangle$), stationary mode ($\square$), unsteady component ($\bigcirc$) measured at $z = 1.3$ with two edge Reynolds numbers, $R_{edge} = 618, 731$ (IP01, IP02) cases, respectively. The chain lines in (*a–d*) show the Reynolds number for onset of absolute instability.

of local absolute instability and that has a secondary absolute instability, Viaud, Serre & Chomaz's (2008) DNS for an open rotating cavity considered the global-stability characteristics. Their figure 5(*b*) can be compared with figure 8(*a,b*) here, showing similar behaviour at the primary front.

A notable feature in figures 8(*a*) 8(*b*) is that while the total disturbance amplitudes (v_{rms}) for the two measurement cases correspond very well, as shown in figure 4(*a*), the relative amplitudes of the stationary and unsteady disturbances ($v_{rms,st}$ and $v_{rms,us}$, respectively), which together form v_{rms} differ for the two cases. This perhaps indicates that the travelling disturbances (via absolute instability) lead the flow to nonlinear saturation irrespective of the amplitude of the stationary cross-flow vortices, which do not themselves become absolutely unstable but which are unavoidably excited in experiments and are convectively unstable. Here, we suggest that figure 8(*a,b*) shows a primary nonlinear steep-fronted travelling global mode at the boundary between the local convectively and absolutely unstable regions of rotating-disk flow, with nonlinear saturation determined by the primary travelling mode, overlaying the saturation (at lower amplitude) of the primary convectively unstable stationary mode. As in Viaud *et al.*'s (2008) figure 5(*b*), figure 8(*a,b*) shows the primary front straddling R_{CA} such that the upstream tail of the front lies in the convectively unstable region, $R < 507$, showing a smooth mapping from the convective to absolute regimes.

As shown in § 3.3 and this section, even for very smooth clean disks, the stationary vortices are unavoidable in experimental studies but they complicate the interpretation of results and comparison with results from numerical and theoretical global-stability studies. The stationary vortices modulate the base flow and it is still unclear how the mean-flow modulation affects the global behaviour, for example, the critical global frequency. However, as discussed by Imayama *et al.* (2013), it seems likely that sufficiently rough disks could exhibit alternative laminar–turbulent transition mechanisms based on the convectively unstable stationary vortices below the critical Reynolds number for absolute instability. Here, what we can venture tentatively is that in order to observe experimentally the 'clean'-disk route with this steep nonlinear global mode that saturates and leads to turbulent breakdown, the total disturbance amplitude at the primary front at $R = 507$ ($v_{rms,507}$), should not exceed the value of the amplitude shown consistently here, i.e. $v_{rms,507}$ should be less than ~ 0.01 at $z = 1.3$.

3.5. *Time series due to stationary and unsteady disturbances*

To distinguish characteristics of stationary from travelling disturbances and other unsteady components, ensemble-averaged and unsteady time series are presented in this section. It is shown that the unsteady time series capture signs of secondary instability at certain wall-normal heights and Reynolds numbers.

Time series of the azimuthal fluctuation velocity measured using hot-wire or hot-film anemometry have been shown in many early studies (Smith 1947; Kobayashi *et al.* 1980; Malik *et al.* 1981; Kohama 1984; Wilkinson & Malik 1985; Le Gal 1992; Kohama *et al.* 1994; Jarre *et al.* 1996; Lingwood 1996; Corke & Knasiak 1998; Imayama *et al.* 2013). These measurements have elaborated on the primary stationary instabilities of the boundary-layer flow and, to a lesser extent, secondary instabilities.

Figure 9 shows unsteady and stationary time series with p.d.f.s calculated using the full (unaveraged) time-series records measured at $z = 1.3$ at intervals of $\Delta R = 20$ between $R = 530$ and 630, i.e. PP07–12 cases. The unsteady time series in figure 9 show data where the stationary (ensemble-averaged) time series have been subtracted from arbitrarily selected instantaneous time series from single revolutions of the disk. At $R = 530$ the ensemble-averaged time series is amplitude modulated, which corresponds to azimuthal variation in the amplitude of the stationary disturbances caused by superposition of disturbance fields generated by the inhomogeneous distribution of unavoidable minute surface roughness. Figure 6(b) shows that at $R = 530$ the spectrum has the fundamental frequencies and two harmonics, indicating nonlinearity. The nonlinear effects are, however, still small at this Reynolds number and are not obvious in figure 9(a).

Figure 9 also shows p.d.f.s of azimuthal fluctuation velocity. These correspond to those used in the p.d.f. maps in Imayama *et al.* (2012). Note that the p.d.f. of a sinusoidal wave has two symmetric maxima. The p.d.f. in figure 9(a), however, shows one maximum located at almost zero because of the amplitude modulation of the time series. The p.d.f. in figure 9(b) shows two maxima, which indicates that the full single-realization time series at $R = 550$ has a much more constant amplitude than at $R = 530$ in figure 9(a). This behaviour agrees with the flatness distribution discussed in § 3.2, figure 4(d), showing that the flatness becomes close to 1.5 as the Reynolds number approaches 550 (a sign of a near-sinusoidal signal).

Comparing time series at $R = 550$–570, the amplitudes of the unsteady time series increase and the shape becomes sharper, whereas the amplitudes of the ensemble-averaged time series are nearly constant. This sharpening of the signal
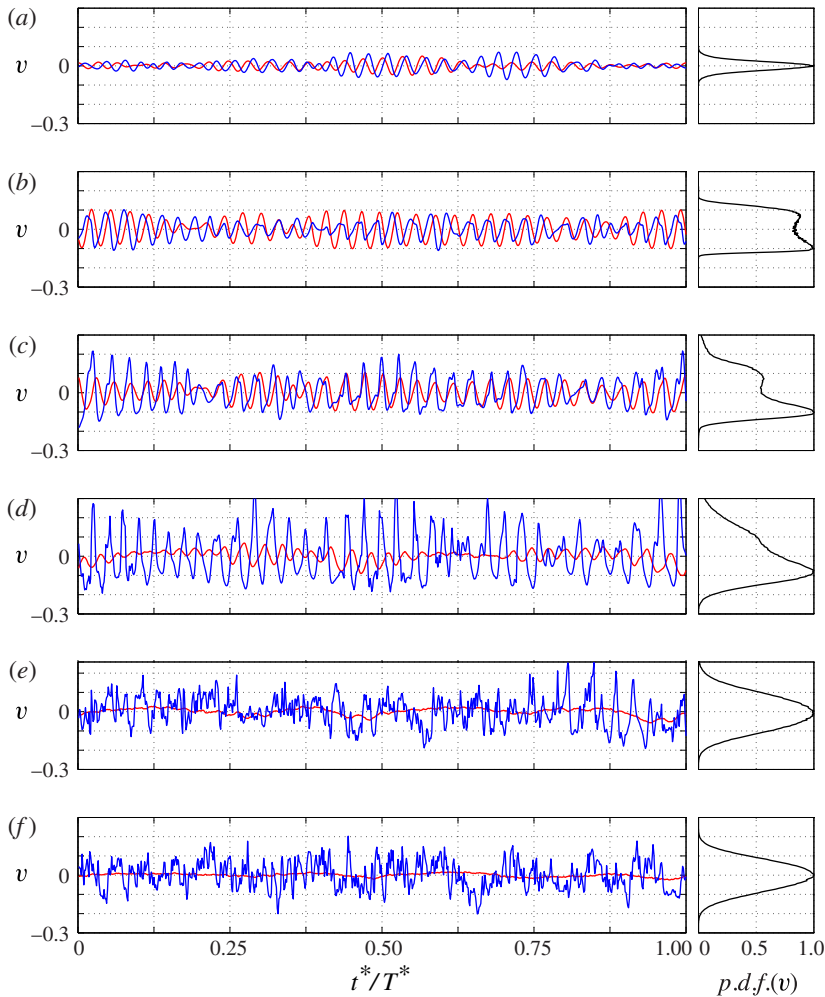
FIGURE 9. Unsteady (blue) and stationary (red) time series of normalized azimuthal fluctuation velocity and probability density function (p.d.f.) calculated using in each case the full instantaneous time series record (unaveraged) measured at $z = 1.3$: (*a*) $R = 530$, (*b*) $R = 550$, (*c*) $R = 570$, (*d*) $R = 590$, (*e*) $R = 610$, (*f*) $R = 630$. Stationary time series are constructed from ensemble-averaged time series and unsteady time series are constructed by subtracting ensemble-averaged time series from instantaneous time series which are arbitrarily selected for one revolution of the disk. The range of the ordinate is -0.3 to 0.3. t^* and T^* are time and a period of one disk revolution, respectively. Each p.d.f. is normalized by the maximum value.

shape in the unsteady time series skews the p.d.f.s. This change accords with nonlinear saturation of the stationary mode at $R = 550$–570, whereas the total disturbance amplitudes, including the unsteady components, continue growing up to about $R = 585$; see figure 8. Finally, figure 9(*d*) at $R = 590$ shows the amplitude of the ensemble-averaged time series decreasing with turbulent breakdown of the stationary mode. At $R = 610$ (figure 9*e*) ensemble-averaged time series show some evidence of modulation with a period of 1/4 of the period of disk rotation. A phenomenon with
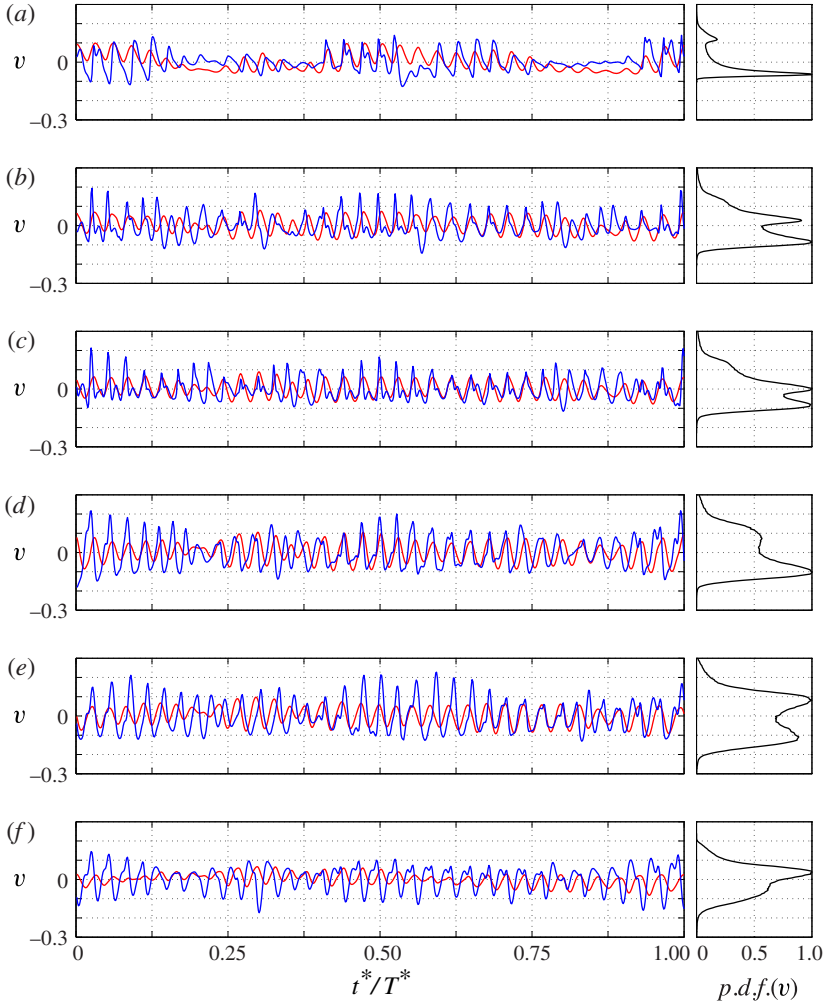
FIGURE 10. Unsteady (blue) and stationary (red) time series of normalized azimuthal fluctuation velocity and probability density function (p.d.f.) calculated using in each case the full instantaneous time series record (unaveraged) measured at $R = 570$: (*a*) $z = 3.0$, (*b*) $z = 2.0$, (*c*) $z = 1.8$, (*d*) $z = 1.3$, (*e*) $z = 1.0$, (*f*) $z = 0.6$. Time is t^* and T^* is the period of one disk revolution. The range of the ordinate is -0.3 to 0.3. Each p.d.f. is normalized by the maximum value.

this periodicity was captured in the flow visualizations of Kobayashi *et al.* (1980) and investigated by Corke & Knasiak (1998). Unsteady time series at $R = 610$ and above are dominated by the turbulent signal component and the p.d.f. becomes increasingly Gaussian.

These changes in the unsteady time series as a function of Reynolds number in figure 9 are similar to the observations in Lingwood (1996) (see her figure 7), where no obvious sign of secondary instability was captured in either single-realization or ensemble-averaged time series. However, figure 10 presents unsteady time series and ensemble-averaged time series measured at different wall-normal heights at $R = 570$ and captures in the unsteady time series the characteristic kinked fluctuation velocity
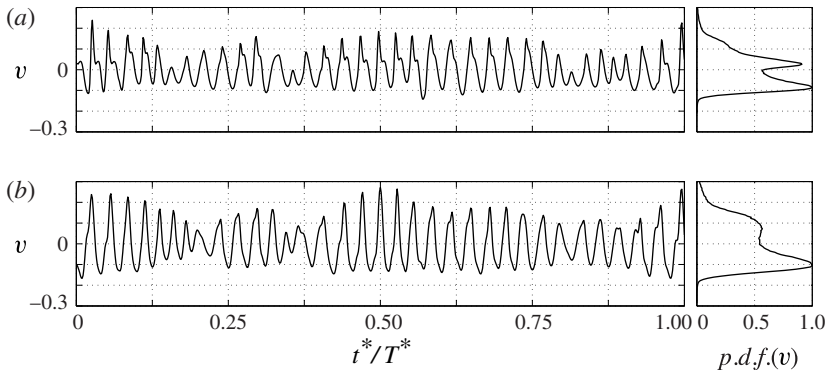
FIGURE 11. A single-realization time series of normalized azimuthal fluctuation velocity and p.d.f. calculated using in each case the full time-series record (unaveraged) measured at $R = 570$: (*a*) $z = 2.0$, (*b*) $z = 1.3$. Time is t^* and T^* is the period of one disk revolution. The range of the ordinate is -0.3 to 0.3. Each p.d.f. is normalized by the maximum value.

not at $z = 1.3$ but at lower and higher heights. The kinks at $z = 1.8$, 2.0, 3.0 lie on the downward slope of the primary fluctuation; at $z = 0.6$, 1.0 they lie on the upward slope of the primary fluctuation. Note that instantaneous single-realization time series of the total disturbance field show the same features (see figure 11) and therefore they are not an artefact of the subtraction of the ensemble-averaged signal. Importantly, however, ensemble-averaged time series do not show such features, indicating that the secondary instabilities associated with the kinks are travelling and, therefore, averaged away by the ensembling process. Lingwood's (1996) measurements were taken at $z = 1.3$ whereas Kobayashi *et al.* (1980) and Wilkinson & Malik (1985), who observed kinks in their time series, measured at $z = 1.77$ instead. These results suggest, contrary to Lingwood (1996), that secondary instability plays a role in the turbulent-breakdown process after the onset of absolute instability. The appearance of the secondary instability corresponds to the rapid growth of the high-frequency components in the spectra shown in figure 5(*a*). This observation agrees with Viaud *et al.*'s (2011) suggestion that global instability of the primary mode leads to secondary instability a little downstream of the primary front (the boundary between convective and absolute instability) and 'this secondary instability leads to a very disorganized state, defining the transition to turbulence'.

Furthermore, Imayama *et al.* (2012) constructed p.d.f. maps from azimuthal fluctuation velocity profiles at $R = 570$ in their figure 7(*f*) to reveal the vertical structure of the primary instability and secondary instability. Figure 11 shows the p.d.f.s corresponding to the single-realization time series measured at two wall-normal heights and using identical data to Imayama *et al.* (2012). Comparing the time series and the p.d.f.s in figure 11(*a*), it is clear that the upper peak in the p.d.f.s can be attributed to the kinked feature of the time series; the p.d.f. in figure 11(*b*) at $z = 1.3$, however, does not show this feature nearly so clearly.

Viaud *et al.*'s (2011) figure 6 shows the vorticity field from DNS within an open rotating-disk cavity, and just before the turbulent-breakdown region there are several small structures (presented in black) located close to the disk surface and seeming to sit on the primary vortices. If these structures are attributed to the secondary instability, then the secondary instabilities reported here close to the wall could correspond to their results. Pier (2003) performed a theoretical study of the

rotating-disk flow and suggested that saturated travelling cross-flow vortices beating at the global frequency (i.e. the frequency of the critical mode at the boundary between local convective and absolute instability) are also absolutely unstable to the secondary perturbations, and concluded that 'transition to a turbulent flow is triggered by secondary absolute instability while the transition location itself is controlled by primary absolute instability'. The difference between the results of Viaud *et al.* (2011) and Pier (2003) is largely that the latter found that the secondary instability with largest absolute growth rate is a subharmonic mode whereas Viaud *et al.*'s (2011) secondary instability is not subharmonic.

The results presented here and by Imayama *et al.* (2013) broadly agree with Viaud *et al.* (2011) and Pier (2003) with emergence of nonlinearity being highly reproducible at the boundary of convective and local absolute instability, i.e. at the primary front, as shown in Imayama *et al.* (2013) and the secondary instability appearing downstream and leading rapidly to a disorganized state. Unfortunately measurements using a single hot-wire probe fixed in the laboratory frame cannot easily capture the characteristics of the travelling secondary instabilities such as the frequency and growth rate. Further research would be required to characterize these instabilities fully.

When the surface of the disk is sufficiently rough an alternative transition mechanism has been proposed, e.g. Lingwood (1996), Healey (2010), Harris *et al.* (2012), Garrett *et al.* (2012), Imayama *et al.* (2013). Table 3 in Imayama *et al.* (2013), which sorts 'clean' and 'rough' disk experiments, suggests that Kobayashi *et al.*'s (1980) results could show a lower-Reynolds-number convective transition route caused by high initial disturbance levels. While their kinked fluctuation velocity at $R = 500$ shown in their figure 9(*d*) is somewhat similar to the secondary instability shown here at $R = 570$, it is likely that their secondary instability is due to large convective growth of the stationary vortices. However, the difference between the secondary instability of these two transition mechanisms is still not clear and further research on the travelling global mode and its secondary instability is required.

3.6. *Growth of stationary disturbances and their turbulent breakdown*

In this section, the stationary vortices and their turbulent breakdown are studied and are related to the flow visualizations by Kobayashi *et al.* (1980), which showed stationary vortices and sharp turbulent transition at a well-defined Reynolds number. Figure 12 shows ensemble-averaged azimuthal fluctuation velocities measured at $z = 1.3$; each positive and negative region represents a stationary vortex. Visually, figure 12(*a*) captures the characteristics of turbulent transition as well as Kobayashi *et al.*'s (1980) flow visualizations.

Figure 12(*a*) presents the growth in disturbance amplitude with increasing Reynolds number of the stationary vortices, and the amplitude suddenly drops indicating turbulent breakdown. Outward of turbulent breakdown, there are signs of stationary structures with four oscillations per revolution, as observed in Kobayashi *et al.*'s (1980) figure 7; see also Corke & Knasiak (1998). Close inspection of the spectra shows corresponding peaks at ω^*/Ω^* of between 4 and 6. It is important to note that although each stationary vortex has a different amplitude at the radial location of turbulent breakdown, that radial location (or Reynolds number) is the same for all, namely turbulent breakdown is controlled by Reynolds number rather than individual vortex amplitudes; this is shown more clearly by figure 13.

Figures 12(*b*) and 12(*c*) show the same quantities as figure 12(*a*) but presented in Cartesian coordinates, with $R_{edge} = 618$ and 731, i.e. IP01 and IP02 cases, respectively.
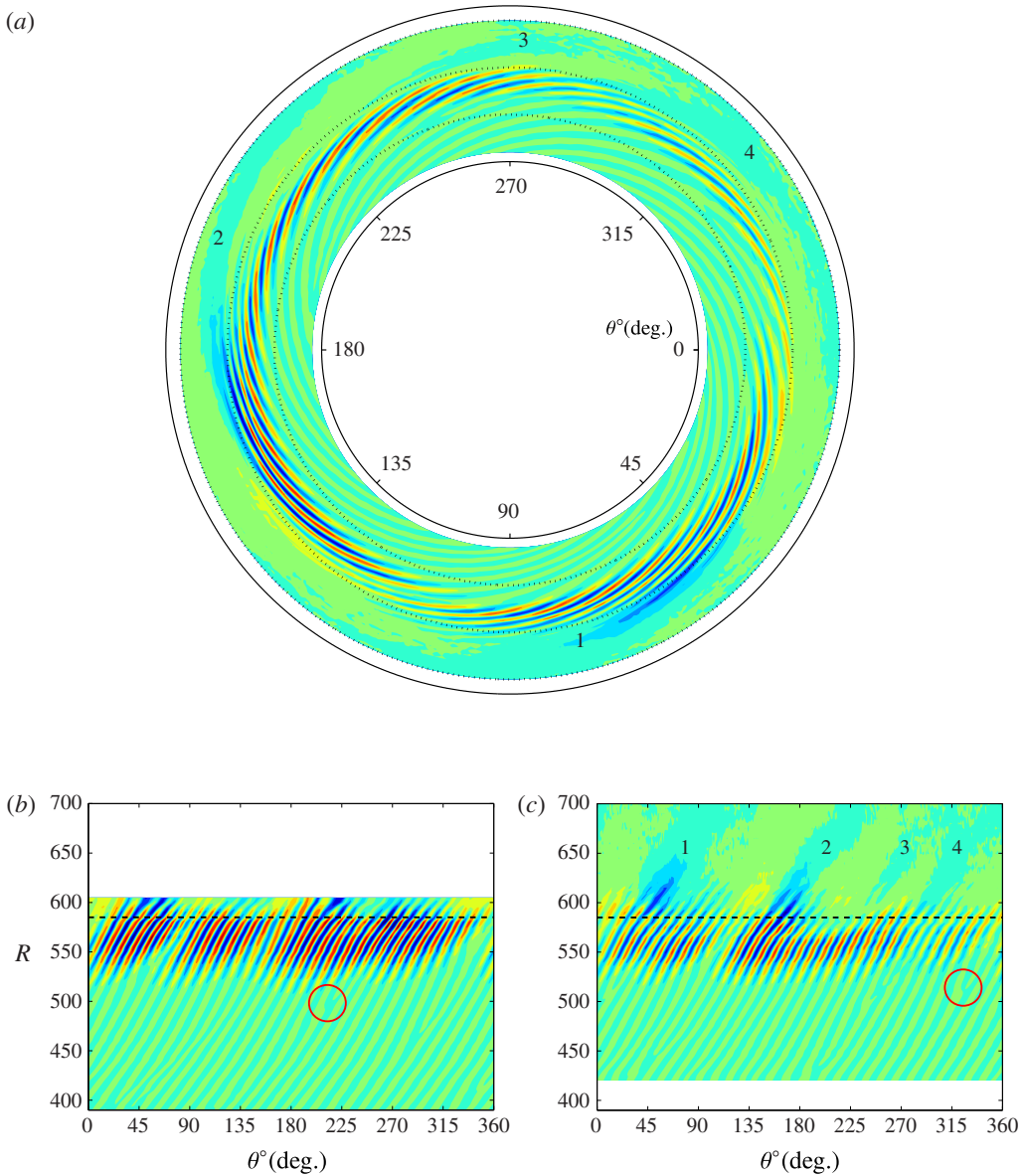
FIGURE 12. Stationary-vortex distributions measured at $z = 1.3$ with a radial step of $\Delta R = 5$: (*a*) $R_{edge} = 731$ (polar coordinates and with the disk rotating anti-clockwise); (*b*) $R_{edge} = 618$ (IP01); (*c*) $R_{edge} = 731$ (IP02). The filled contours from blue to red indicate -0.12, -0.1, -0.08, -0.06, -0.04, -0.02, 0, 0.02, 0.04, 0.06, 0.08, 0.1, 0.12 of the ensemble-averaged fluctuation velocity normalized by the local wall speed. In (*a*), dotted lines indicate $R = 500$, 600, 700, respectively moving outward, and outer solid circle line indicates edge of the disk (i.e. $R = 731$). Horizontal dashed lines at $R = 585$ in (*b*,*c*) indicate Reynolds number of maximum amplitude of v_{rms} shown in figure 8(*a*,*b*). Labels 1–4 in (*a*) and (*c*) mark stationary structures and red circles in (*b*) and (*c*) highlight example vortex-splitting events.
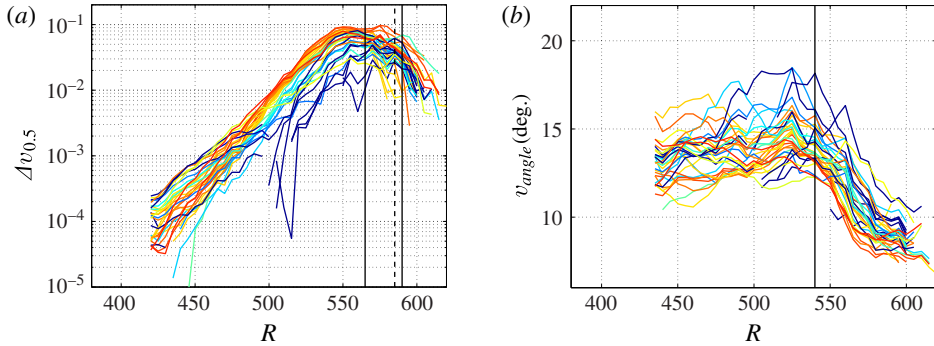
FIGURE 13. Tracking individual stationary vortices for $R_{edge} = 731$ (IP02), same data as in figure 12(c). (a) $\Delta v_{0.5}$ of each stationary vortex. The colour indicates the amplitude of $\Delta v_{0.5}$ at $R = 500$ as a reference amplitude. Vertical solid lines at $R = 565, 590$ indicate the region of rapid growth of the high-frequency component shown in figure 5(a). Vertical dashed line at $R = 585$ indicates the Reynolds number of maximum amplitude of v_{rms} shown in figure 8(a,b). (b) The angle distributions of each stationary vortex. The colour indicates the reference amplitude used in (a). Vertical solid line at $R = 540$ indicates where the wave angle of the stationary vortices starts decreasing.

These results show clearly the near-constant turbulent-breakdown Reynolds number independent of the stationary-vortex amplitudes. The contour colours in the nonlinear saturation region (i.e. $R = 550$–570) in figure 12(c) are lighter than in figure 12(b) because the nonlinear saturation amplitude of the stationary mode is smaller, for this R_{edge}, as shown in figure 8(a,b) (although the saturation of the total disturbance field is shown to be independent of R_{edge}). In addition, comparing figure 12(b,c) to Kawakami, Kohama & Okutsu's (1999) figures 3 and 7, which are without and with artificial roughnesses, respectively, differences in the breakdown of the cross-flow vortices between the rotating-disk flow and swept-wing flow are clearly observable.

Corresponding to the observation, for example, by Wilkinson & Malik (1985), figure 12(b,c) also shows the stationary vortices 'splitting' as the Reynolds number increases; see, for example, the regions marked by red circles. In our experiments, we find an increase in the number of stationary vortices from 27 to 34 over the range $R = 400$–575. This increase with Reynolds number corresponds to the increase in the most unstable azimuthal wavenumber for stationary disturbances from linear stability theory (see Pier 2003).

To investigate details of each stationary vortex, figure 13 shows individually the amplitude growth of each vortex and each vortex angle. Here, the amplitude, $\Delta v_{0.5}$ is measured at $z = 1.3$ so that $\Delta v_{0.5}$ gives half of the peak-to-peak amplitude of each stationary vortex. The wall-normal height of $z = 1.3$ was chosen as this is where the maximum amplitude of the stationary-disturbance r.m.s. profile (see figure 7) is observed. The colour indicates the amplitude at $R = 500$, showing the range of amplitudes (blue lowest and red highest) at this location. At $R \leqslant 470$–480 the individual stationary-vortex amplitudes do not necessarily develop maintaining the same ordering as they have at $R = 500$. This is because the stationary vortices are excited not by only one roughness but by unavoidable, minute roughnesses distributed across the disk surface, and this distribution affects the relative amplitudes until each vortex has grown sufficiently. However, for $R > 470$–480 each stationary vortex then grows exponentially. At $R = 550$, nonlinear saturation is observed with amplitudes

of $\Delta v_{0.5} = 0.015$–0.1. Typically, nonlinear saturation amplitudes of stationary vortices in swept-wing flows are about $\Delta v_{0.5} = 0.3$ (Kawakami *et al.* 1999) or 0.16–0.22 (Chernoray *et al.* 2005), which are higher than those found here for the rotating-disk flow.

Figure 13(*a*) shows that the stationary vortices undergo turbulent breakdown, indicated by the decrease in their amplitude after nonlinear saturation, at almost constant Reynolds number, $R = 570$–580, despite the variation in their amplitudes at $R = 500$ of almost one order of magnitude. $R = 570$–580 corresponds to the appearance of travelling secondary instabilities presented in figure 10 and subsequent rapid growth in the high-frequency range shown in figure 5(*a*). These results indicate that turbulent breakdown of the stationary vortices is triggered not by their amplitude but by another mechanism, which could be growth of travelling disturbances instead.

Another interesting characteristic of the stationary vortices is captured by investigating their angles to the azimuthal direction. The stationary vortex angle, v_{angle}, is defined as the angle between the axis of the stationary vortex and the azimuthal coordinate, see e.g. equation 1 in Wilkinson & Malik (1985). Figure 13(*b*) shows the angle of each stationary vortex with the colours corresponding to those in figure 13(*a*). In general, the angle increases with Reynolds number up until $R = 540$ where it then decreases to turbulent breakdown. This change of the angle corresponds to the onset of nonlinear saturation of the stationary vortices shown in figure 8(*a*,*b*) and where the boundary layer starts to thicken as shown in 2(*a*). Indeed, $R = 540$ is where local the azimuthal mean velocity profile first shows significant deformation due to the stationary vortices.

Note that the change in angle for each stationary vortex at $R = 540$ is independent of its amplitude, which suggests that this change in the stationary structure and the nonlinear saturation may be triggered by the growth of the travelling mode through nonlinear interaction. Namely, these results suggest that the convective instability of the stationary mode and the consequent amplitude growth do not control turbulent breakdown. Instead, it would appear that above $R = 507$ nonlinear interaction between stationary and travelling disturbances may control the breakdown consistently in Reynolds number, independent of azimuthal location.

4. Conclusions

The laminar–turbulent transition of the incompressible rotating-disk flow has been investigated experimentally using hot-wire anemometry. The surface of the disk is smooth and is considered to be well within the 'clean' category of experimental facilities. No artificial forcing is applied to the boundary-layer flow. The measured laminar mean velocity profiles and associated characteristics agree very well with theoretical values. To investigate disturbance growth, azimuthal velocity measurements are taken at constant wall-normal height ($z = 1.3$) and at intervals of $\Delta R = 5$ from the laminar to the turbulent region for two different edge Reynolds numbers. The edge Reynolds number does not appear to affect the total-amplitude growth, total nonlinear saturation nor the final turbulent breakdown.

Power spectra show that the azimuthal fluctuation velocities in the instability region are not only composed of stationary disturbances but also of unsteady disturbances. The radial growth rate of the stationary disturbances corresponds to local linear theoretical analysis (e.g. Hussain *et al.* 2011). As previously shown by Imayama *et al.* (2013), the onset of nonlinearity is highly reproducible at $R = 510$–520 across the various experimental conditions, supporting the theoretical finding that radial

absolute instability above $R = 507$ triggers the nonlinearity as the first step towards laminar–turbulent transition. In the present study, we show that the radial growth rates of both stationary and unsteady disturbances consistently decrease beyond $R \approx 507$ due to nonlinear interactions. It is not possible to identify frequency components in the spectra corresponding exactly to the absolute/global frequency predicted from theoretical analyses around $\omega^*/\Omega^* = 50.3$ but here a travelling-mode contribution centred on $\omega^*/\Omega^* \approx 40$ is clearly observed (particularly noticeable at high z). It is possible that this corresponds to the global mode realized in the physical flow, which is inevitably more complex than the base flow considered in theoretical analyses, e.g. due to convectively unstable stationary vortices. Other effects presumably attributable to the absolute instability are also observed, in particular at the later stage of laminar–turbulent transition.

In the nonlinear region, the harmonic parts of the spectra grow and the stationary vortices saturate at $R = 550$ whereas the travelling mode continues to grow up to $R = 585$. The nonlinear saturation amplitude for the stationary vortices shows some dependence on edge Reynolds number and/or on other differences in the natural excitation of stationary disturbances between different cases; however the total disturbance amplitude at saturation is constant for all cases, which is perhaps due to compensations made by the travelling global-mode and secondary-instability contributions.

Investigations of the growth of individual stationary vortices show that their nonlinear saturation and turbulent breakdown are independent of their amplitudes, which vary azimuthally dependent on their convective-growth history, and instead their late-stage breakdown behaviour is determined by well-defined Reynolds numbers. For example, irrespective of individual vortex amplitudes, at $R = 540$ the wave angle starts to decrease and the amplitude of each stationary vortex starts to saturate. Furthermore, for the stationary vortices turbulent breakdown occurs at $R = 570$–580 approximately homogeneously in the azimuthal direction despite individually varying vortex amplitudes. These results show that convective growth and resulting amplitude of the stationary mode is not fundamentally important to fixing the final turbulent breakdown. At $R = 570$ unsteady time series capture signs of travelling secondary instabilities characterized by kinked azimuthal fluctuation velocity. We note that the secondary instabilities are not clearly observed at $z = 1.3$ but are above and below this wall-normal height. At higher R, the flow becomes very disordered leading rapidly to turbulence. Power spectra capture a jump in disturbance energy at high frequencies between $R = 565$–590. These results correspond to Viaud *et al.*'s (2011) direct numerical simulations of an open rotating-cavity flow and transition to turbulence through a steep-nonlinear global mode with a secondary global mode leading to turbulence.

We hypothesize that the (travelling) global mode emerges as a result of the local absolute instability at $R = 507$ and develops nonlinearly interacting with convectively unstable stationary vortices, which unavoidably are found to have finite amplitude by $R = 507$ (as shown by figure 6), creating a primary front for the total disturbance field comprising travelling and stationary disturbances. The behaviour of the front appears to be insensitive to variations in edge Reynolds number and variations in the amplitude of the stationary-disturbance field from case to case; the fronts for the total disturbance field from different cases collapse onto each other as do the total nonlinear saturation amplitudes at about $R = 585$ (see figure 4). In fact, from $R \approx 550$ the front for the total disturbance field is dominated by unsteady components presumably due to the travelling global mode (see figure 8). This may determine the nonlinear saturation of
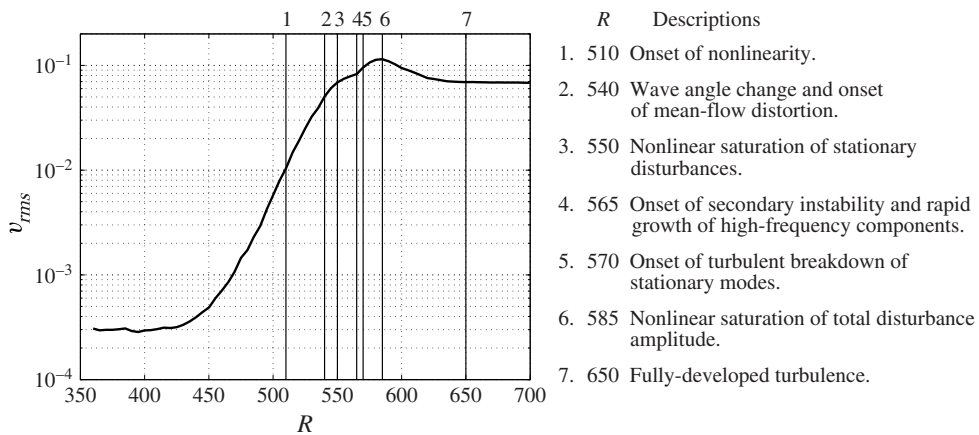
	R	Descriptions
1.	510	Onset of nonlinearity.
2.	540	Wave angle change and onset of mean-flow distortion.
3.	550	Nonlinear saturation of stationary disturbances.
4.	565	Onset of secondary instability and rapid growth of high-frequency components.
5.	570	Onset of turbulent breakdown of stationary modes.
6.	585	Nonlinear saturation of total disturbance amplitude.
7.	650	Fully-developed turbulence.

FIGURE 14. Summary of the laminar–turbulent transition process for 'clean' disk conditions. The figure shows azimuthal disturbance growth as a function of Reynolds number (IP02). The vertical solid lines and numbers show the Reynolds number at which specific characteristics of the transition process are observed in this study, as summarized to the right of the figure.

the stationary vortices and their subsequent secondary instability starting at $R \approx 565$ and turbulent breakdown above $R = 570$–580, leading to fully developed turbulence above $R = 650$.

The results presented support, for example, Lingwood (1995), Pier (2003) and Viaud *et al.* (2011), and do not discount the possibility of a global linear instability as proposed by Healey (2010) caused by the finite disk radius, leading directly to a nonlinear global mode. In summary, figure 14 shows the key Reynolds-number values for steps in the laminar–turbulent transition of the rotating-disk flow for 'clean' disk conditions, as determined from the experiments described herein.

Acknowledgements

Appendix

In § 3.3, we apply a moving average to the spectra to smooth out the spikes observed at integer values of ω^*/Ω^* at Reynolds numbers where the stationary disturbances are unstable. These spikes have also been observed in other experimental studies of rotating-disk flow (e.g. Imayama, Alfredsson & Lingwood 2011; Siddiqui *et al.* 2013), where high-resolution spectra have been produced. In this study, it is suggested that the integer spikes in the spectra indicate the stationary disturbances whereas the relatively smooth peaked regions of the primary and its harmonics are due to travelling disturbances. Figure 15(*a*) shows spectra of single-realization and ensemble-averaged time series measured at $z = 4.0$ and $R = 530$, where the single-realization data correspond to those shown in figure 6(*e*). Figure 15(*b*) is a magnification of the spectra, showing that the spikes are located at each integer value
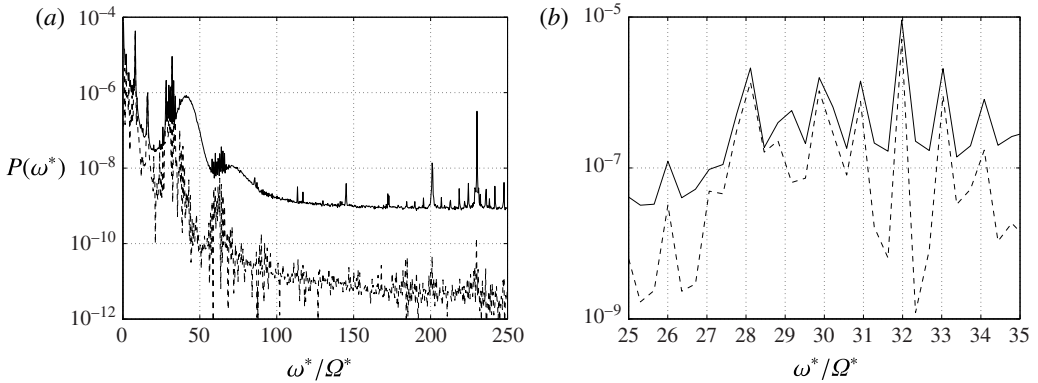
FIGURE 15. (*a*) Spectra of single-realization (solid line) and ensemble-averaged (dashed line) time series at $z = 4.0$ and $R = 530$. (*b*) A close-up view of the spectra in (*a*) over a smaller frequency range.

of ω^*/Ω^* (small misalignment of the spikes with exact integer numbers is due to the resolution of Fourier transformation). It is clear that spikes in the spectrum of the ensemble-averaged time series (which only shows the frequency content of the stationary disturbances) correspond to spikes in the single-realization spectrum; other features of the single-realization spectrum, such as the smooth peak centred at about $\omega^*/\Omega^* = 40$, correspond to travelling disturbances.

The inhomogeneous distribution of surface roughness on the disk excites disturbances that are stationary in the rotating frame, creating a superposition of unstable vortices with integer azimuthal wavenumbers (the azimuthal wavenumbers taking integer values because of the azimuthal periodicity of the configuration). The superposition of integer-wavenumber stationary disturbances creates an amplitude-modulated and wavenumber-modulated signal, where the wavenumber modulation is fixed by the azimuthal periodicity. The hot-wire probe in the lab frame interprets this wavenumber modulation as a frequency-modulated time series, i.e. the frequencies it detects are a conflation of the azimuthal wavenumbers and perturbation frequencies in the rotating frame. Because the stationary disturbances have zero frequency in the rotating frame, by definition, integer frequency values in the stationary component of the measured frequency-modulated time series correspond to integer azimuthal wavenumber values. Here, the Fourier transform of a frequency-modulated time series is given to demonstrate the explanation above. A sinusoidal time series v_{sin} is defined as

$$v_{sin} = \sin(w_1 t), \qquad (A\,1)$$

to compare with frequency-modulated signal, where w_1 is the frequency set to have 30 oscillations for one period, T, to simulate 30 stationary vortices. Furthermore, the frequency-modulated time series v_{FMS} is defined as

$$v_{FMS} = \sin(w_1 t + \cos(w_2 t)), \qquad (A\,2)$$

where w_2 is a modulation frequency set to have frequency modulation in a period of T corresponding to one disk revolution time. A frequency-modulated signal such as this results from a superposition of sinusoids periodic in T. Figure 16 shows v_{sin} and v_{FMS}. Figure 17 gives the power spectra of these signals showing clearly spikes (at integer
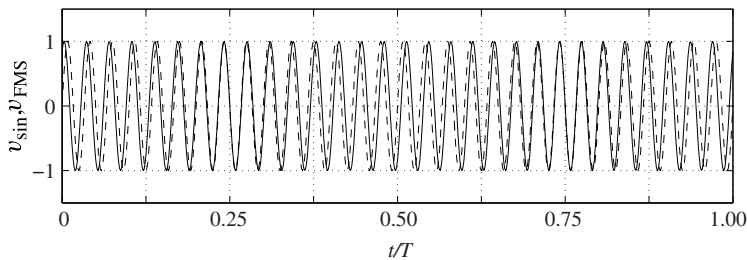
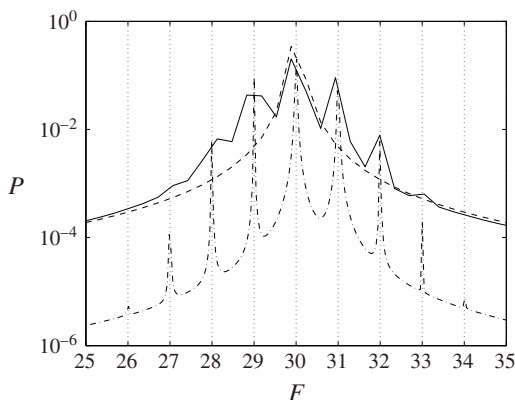FIGURE 16. Sinusoidal (dashed line) and frequency-modulated (solid line) signal in one period *T*.

FIGURE 17. Power spectra of the sinusoidal and frequency-modulated signals v_{sin} (dashed line) and v_{FMS} (solid line). The chain line is the high-resolution power spectrum of the frequency-modulated signal. *F* is the normalized frequency.

values of normalized frequencies) in the frequency-modulated spectrum, as observed in the spectra from the experimental data for stationary disturbances (see figure 15).

REFERENCES

BALACHANDAR, S., STREETT, C. L. & MALIK, M. R. 1992 Secondary instability in rotating-disk flow. *J. Fluid Mech.* **242**, 323–347.

CHAM, T.-S. & HEAD, M. R. 1969 Turbulent boundary-layer flow on a rotating disk. *J. Fluid Mech.* **37**, 129–147.

CHERNORAY, V. G., DOVGAL, A. V., KOZLOV, V. V. & LÖFDAHL, L. 2005 Experiments on secondary instability of streamwise vortices in a swept-wing boundary layer. *J. Fluid Mech.* **534**, 295–325.

CHOMAZ, J.-M. 2005 Global instabilities in spatially developing flows: non-normality and nonlinearity. *Annu. Rev. Fluid Mech.* **37**, 357–392.

CORKE, T. C. & KNASIAK, K. F. 1998 Stationary travelling cross-flow mode interactions on a rotating disk. *J. Fluid Mech.* **355**, 285–315.

DAGENHART, J. R. & SARIC, W. S. 1999 Cross-flow stability and transition experiments in swept-wing flow *NASA/TP*-1999-209344.

DAVIES, C. & CARPENTER, P. W. 2003 Global behaviour corresponding to the absolute instability of the rotating-disc boundary layer. *J. Fluid Mech.* **486**, 287–329.

FALLER, A. J. 1991 Instability and transition of disturbed flow over a rotating disk. *J. Fluid Mech.* **230**, 245.

GARRETT, S. J., HARRIS, J. & THOMAS, P. J. 2012 On the effect of distributed roughness on transition over rotor-stator devices. In *Proc. 28th ICAS Cong. 2012, Brisbane, Australia* (ed. I. Grant), pp. 1–8.

GREGORY, N., STUART, J. T. & WALKER, W. S. 1955 On the stability of three-dimensional boundary layers with application to the flow due to a rotating disk. *Phil. Trans. R. Soc. Lond.* **248**, 155–199.

HARRIS, J., GARRETT, S. J. & THOMAS, P. J. 2012 On the stability of flows over rough rotating disks *AIAA Paper* 2012-3075, pp. 1–11.

HEALEY, J. J. 2010 Model for unstable global modes in the rotating-disk boundary layer. *J. Fluid Mech.* **663**, 148–159.

HUSSAIN, Z., GARRETT, S. J. & STEPHEN, S. O. 2011 The instability of the boundary layer over a disk rotating in an enforced axial flow. *Phys. Fluids* **23**, 114108.

IMAYAMA, S., ALFREDSSON, P. H. & LINGWOOD, R. J. 2011 An experimental study of laminar-turbulent transition of a rotating-disk flow In *EUROMECH Colloquium 525, Instabilities and Transition in Three-Dimensional Flows with Rotation, Écully, France*, pp. 29–30.

IMAYAMA, S., ALFREDSSON, P. H. & LINGWOOD, R. J. 2012 A new way to describe the transition characteristics of a rotating-disk boundary-layer flow. *Phys. Fluids* **24**, 031701.

IMAYAMA, S., ALFREDSSON, P. H. & LINGWOOD, R. J. 2013 An experimental study of edge effects on rotating-disk transition. *J. Fluid Mech.* **716**, 638–657.

IMAYAMA, S., LINGWOOD, R. J. & ALFREDSSON, P. H. 2014 An experimental study of a rotating-disk turbulent boundary-layer flow. In *Proc. Phys.–iTi Conference on Turbulence* (ed. A. Talamelli, M. Oberlack & J. Peinke), vol. 149, pp. 173–176. Springer.

JARRE, S., LE GAL, P. & CHAUVE, M. P. 1996 Experimental study of rotating disk instability. I. Natural flow. *Phys. Fluids* **8**, 496–508.

VON KÁRMÁN, T. 1921 Über laminare und turbulente Reibung. *Z. Angew. Math. Mech.* **1**, 233–252.

KAWAKAMI, M., KOHAMA, Y. & OKUTSU, M. 1999 Stability characteristics of stationary cross-flow vortices in three-dimensional boundary layer. *AIAA Paper* 99-0811.

KOBAYASHI, R., KOHAMA, Y. & TAKAMADATE, C. 1980 Spiral vortices in boundary layer transition regime on a rotating disk. *Acta Mechanica* **35**, 71–82.

KOHAMA, Y. 1984 Study on boundary layer transition of a rotating disk. *Acta Mechanica* **50**, 193–199.

KOHAMA, Y., SUDA, K. & WATANABE, H. 1994 Traveling disturbances on a spinning disk boundary layer. *Trans. JSME* B **60** (574), 1978–1984.

LE GAL, P. 1992 Complex demodulation applied to the transition to turbulence of the flow over a rotating disk. *Phys. Fluids* A **4**, 2523–2528.

LINGWOOD, R. J. 1995 Absolute instability of the boundary layer on a rotating disk. *J. Fluid Mech.* **299**, 17–33.

LINGWOOD, R. J. 1996 An experimental study of absolute instability of the rotating-disk boundary-layer flow. *J. Fluid Mech.* **314**, 373–405.

LINGWOOD, R. J. 1997a Absolute instability of the Ekman layer and related rotating flows. *J. Fluid Mech.* **331**, 405–428.

LINGWOOD, R. J. 1997b On the impulse response for swept boundary-layer flows. *J. Fluid Mech.* **344**, 317–334.

LINGWOOD, R. J. & GARRETT, S. J. 2011 The effects of surface mass flux on the instability of the BEK system of rotating boundary-layer flows. *Eur. J. Mech. (B/Fluids)* **30**, 299–310.

MALIK, M. R., WILKINSON, S. P. & ORSZAG, S. A. 1981 Instability and transition in rotating disk flow. *AIAA J.* **19**, 1131–1138.

OTHMAN, H. & CORKE, T. C. 2006 Experimental investigation of absolute instability of a rotating-disk boundary layer. *J. Fluid Mech.* **565**, 63–94.

PIER, B. 2003 Finite-amplitude cross-flow vortices, secondary instability and transition in the rotating-disk boundary layer. *J. Fluid Mech.* **487**, 315–343.

PIER, B. & HUERRE, P. 2001 Nonlinear self-sustained structures and fronts in spatially developing wake flows. *J. Fluid Mech.* **435**, 145–174.

SIDDIQUI, M. E., MUKUND, V., SCOTT, J. & PIER, B. 2013 Experimental characterization of transition region in rotating-disk boundary layer. *Phys. Fluids* **25**, 034102.

SMITH, N. H. 1947 Exploratory investigation of laminar-boundary-layer oscillations on a rotating disk. *NACA TN* 1227.

VIAUD, B., SERRE, E. & CHOMAZ, J.-M. 2008 The elephant mode between two rotating disks. *J. Fluid Mech.* **598**, 451–464.

VIAUD, B., SERRE, E. & CHOMAZ, J.-M. 2011 Transition to turbulence through steep global-modes cascade in an open rotating cavity. *J. Fluid Mech.* **688**, 493–506.

WILKINSON, S. P. & MALIK, M. R. 1985 Stability experiments in the flow over a rotating disk. *AIAA J.* **23**, 588–595.